Nuclear Energy Research Initiative (NERI) Project 06-041

NERI Technical Report
Dynamic Simulation and Optimization of Nuclear Hydrogen Production Systems
Final Report

Final Report for
Project DE-FC07-06ID14751
March 2006 - March 2009

Principal Investigator: Paul I. Barton
Co-Principal Investigator: Mujid S. Kazimi

July 2009

MIT Contributors:
Paul I. Barton
Mujid S. Kazimi
Georgios Bollas
Patricio Ramirez Munoz

1 Summary

The main activities performed during this project were:

- developed detailed simulations of heat transfer loops using hyperbolic equations,
- developed a novel simplification of the gas dynamics equations and its validation,
- created and validated a simplified model for the heat transfer loop,
- simulated start-up of the two-loop system,
- validated the simplified system of equations representing the heat transfer loop using RELAP,
- developed a new formulation for the electrolyte-NRTL thermodynamic model and applied it to an extensive database of electrolytes to validate its performance,
- collaborated with ASPEN Technology Inc. to implement refinements of the electrolyte-NRTL model in the aspenONE software,
- studied the implications that exist in fitting binary parameters of excess Gibbs free energy models, such as the NRTL model, using experimental measurements of liquid-liquid, vapor-liquid and vapor-liquid-liquid phase splits,
- developed a new formulation based on a bilevel optimization strategy for accurately and thermodynamically consistently fitting binary parameters to experimentally measured phase equilibrium data,
- developed an optimization framework for thermodynamic data reduction for the development of a self consistent database of thermodynamic properties of sulfuric acid and hydrogen iodide,
- presented 15 papers in peer reviewed scientific conferences,
- published 5 papers in peer reviewed scientific journals.

2 Technical Narrative

This project is part of a research effort to design a hydrogen plant and its interface with a nuclear reactor. This project developed a dynamic modeling, simulation and optimization environment for nuclear hydrogen production systems. A hybrid discrete/continuous model captures both the continuous dynamics of the nuclear plant, the hydrogen plant, and their interface, along with discrete events such as major upsets. This hybrid model makes use of accurate thermodynamic sub-models for the description of phase and reaction equilibria in the thermochemical reactor. Use of the detailed thermodynamic models will allow researchers to examine the process in detail and have confidence in the accuracy of the property package they use. The hybrid model will allow researchers to study plant operations and accident scenarios. Researchers will also be able to use it to conduct parameter estimation studies to identify possible improvements in materials, mechanical design, and safety issues. The seamless connection between modeling, simulation and optimization can help establish optimal control schemes. These schemes can then be tested in the model.

This project deals mostly with the dynamic modeling of the interface between the nuclear reactor and the hydrogen production plant and the thermodynamics of the Sulfur-Iodine thermochemical cycle. A general sketch of the integrated hydrogen production process with two different options for the hydrogen production process (namely: the SI process and the high temperature electrolysis process) is presented in Figure 1. The heat transfer interface is essential to transfer the heat from the nuclear reactor to the chemical processes. This loop guarantees the safety and operability of the process; it physically separates the nuclear reactor

from the hydrogen production plant and decouples their operation by introducing auxiliary heat sources and sinks (not shown in the figure). On the other hand, in the Sulfur-Iodine thermochemical cycle the heat of the nuclear reactor is used in various separation and decomposition sections of the process (H_2SO_4, SO_3 and HI_x decompositions, as well as for the vaporization and separation sections).

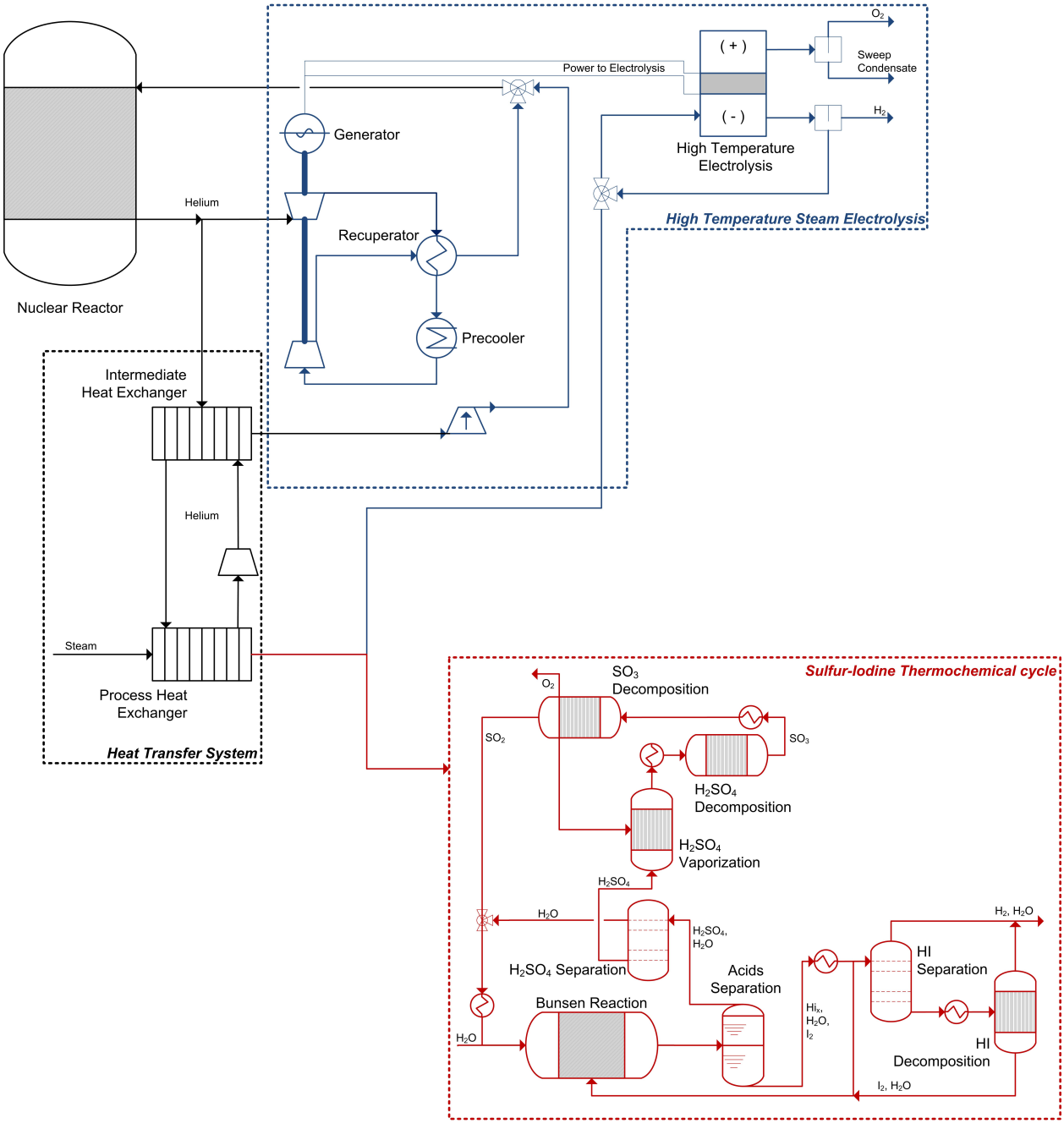

Figure 1: Sketch of integrated nuclear hydrogen production plant.

3 Task 1: Modeling of the heat transfer interface and nuclear reactor

The objective of this research effort was to build dynamic models of various components of the overall nuclear hydrogen production system. Since suitable models must be in place before simulation studies can begin, the majority of the effort was devoted to this task. The overall system model involves models of the nuclear reactor, the interface, the hydrogen production plant and the power conversion unit.

3.1 Overall process structure

Figure 2 shows the flowsheet of the system for the HTSE-PBR-GT configuration. The main components of the process are highlighted: the nuclear reactor, the gas turbine, the heat transfer loop and the high-temperature electrolysis cell. In this case the nuclear reactor provides high-temperature heat for a gas turbine ($\sim$ 90% of the heat) and for the electrolysis cell ($\sim$10% of the heat). The gas turbine produces electricity that will be used to carry out the electrochemical reactions in the electrolysis cell. The heat produced in the nuclear reactor is transferred to the electrolysis cell by the heat transfer loop. This loop guarantees the safety and operability of the process; it physically separates the nuclear reactor from the hydrogen production plant and decouples their operation by introducing auxiliary heat sources/sinks (not shown in the figures). Hydrogen production occurs as follows. Water is first heated and raised to high-temperature steam by the heat exchangers. Then the steam is fed to the electrolysis cell where it is reacted into oxygen and hydrogen. The oxygen is recuperated and the hydrogen/water stream is sent to a steam separator, to be concentrated.

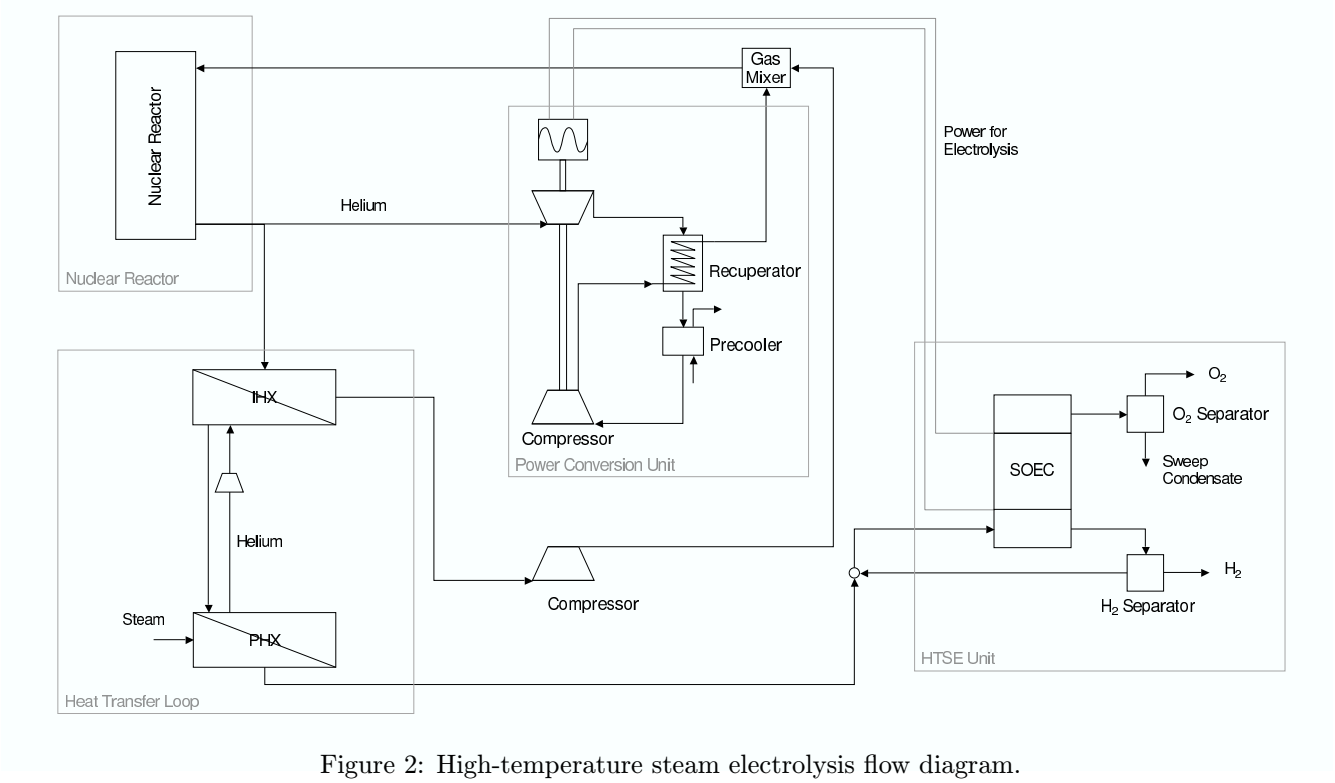

Figure 2: High-temperature steam electrolysis flow diagram.

3.2 Modeling the heat transfer interface

Two decisions were taken regarding the modeling of the heat transfer loop: the number of loops to be used, and the heat transfer fluid. We decided to use two loops and helium as the heat transfer fluid. Helium is the only heat transfer fluid that can provide a safe and reliable operation.

Deriving an adequate set of equations to represent the flow of helium in the pipes and heat exchangers during normal and abnormal operation has been one of the most challenging parts of this project. The inviscid Navier-Stokes equations describe the flow of helium in these situations, and at high Reynolds numbers (significant fraction of the speed of sound) they are a system of quasi-linear hyperbolic partial differential-algebraic equations (PDAEs).

As mentioned above, this involves solving quasi-linear hyperbolic PDAEs in time and in one-spatial dimension on multiple coupled domains (each domain corresponding to an element of the overall heat transfer interface). Previous attempts to simulate similar systems involving a nuclear reactor have used numerical methods that introduce errors and produce unphysical numerical artifacts such as oscillations. Indeed, these numerical artifacts are well understood in the literature on numerical solution of hyperbolic equations [24]. We explored the application of specialized numerical methods for nonlinear hyperbolic equations to produce an accurate representation of the scenarios studied and to predict accurately phenomena such as the formation and propagation of shocks and waves. We realized that such degree of detail is not necessary and we decided to focus on the slow time-scales. For the slow time-scale transients, we used a quasi-steady-state approximation for the equations describing gas flow in a pipe.

One-dimensional flow of helium in the pipes is described by the inviscid Navier-Stokes equations. They are a system of three equations: the continuity equation (conservation of mass), the momentum equation and the energy equation. These equations are called balance laws, because they balance the conservation of the species with the source terms. The source terms considered are the friction in the momentum equation and heat transfer in the energy equation, and they are written as:

- continuity

$$\frac{\partial \rho}{\partial t} + \frac{\partial (\rho v)}{\partial x} = 0, \tag{1}$$

- momentum

$$\frac{\partial \rho v}{\partial t} + \frac{\partial \rho v^2 + P}{\partial x} = \frac{2\rho f v^2}{D}, \tag{2}$$

- energy

$$\frac{\partial \rho e}{\partial t} + \frac{\partial \rho e v + P v}{\partial x} = -\frac{4}{D_T} U (T - T_{ext}). \tag{3}$$

The compressor producing the flow in the heat transfer loop will be represented by quasi-steady-state equations. This equations represent the conservation of mass in the compressor, the compressor characteristic curve, which relates pressure rise in the compressor to mass flow rate and shaft speed (momentum balance) and the efficiency equation, which relates the real gas transformation through the compressor to an ideal isentropic evolution by means of the efficiency factor (energy equation).

3.3 Detailed simulation of the heat transfer loops using hyperbolic equations

Simulating the heat transfer loop involves solving quasi-linear hyperbolic PDAEs in time and in one spatial dimension on multiple coupled domains (each domain corresponding to an element of the overall heat transfer loop). The equations represent the flow of gas in pipes, the heat transfer and the compressor. Previous attempts to simulate similar systems involving a nuclear reactor have used numerical methods that introduce

errors and produce unphysical numerical artifacts such as oscillations. Indeed, these numerical artifacts are well understood in the literature on numerical solution of hyperbolic equations (4-6) [24].

The equations representing the flow of gas in a pipe are the inviscid compressible Navier-Stokes equations:

- continuity

$$\frac{\partial \rho}{\partial t} + \frac{\partial(\rho v)}{\partial x} = 0, \tag{4}$$

- momentum

$$\frac{\partial \rho v}{\partial t} + \frac{\partial(\rho v^2 + P)}{\partial x} = -\frac{2\rho f v|v|}{D}, \tag{5}$$

- energy

$$\frac{\partial \rho e}{\partial t} + \frac{\partial(\rho e v + P v)}{\partial x} = -\frac{4}{D_T} U(T - T_{ext}). \tag{6}$$

The equations representing the compressor are:

- mass conservation equation

$$\rho_{in} v_{in} = \rho_{out} v_{out} \tag{7}$$

- isentropic equation

$$\frac{P_{in}}{P_{out}} = \left(\frac{\rho_{in}}{\rho_{out}}\right)^{\gamma} \tag{8}$$

- dynamic pressure differential

$$P_{out} - P_{in} = \Delta P(t). \tag{9}$$

The numerical solution of these equations was implemented using a Godunov scheme with Roe's Riemann approximate solver, high resolution methods and entropy corrections [24]. A particular challenge was to couple the solution of the compressor equations (Eqs. (7)-(9)) with the explicit method used to solve the gas dynamics. The explicit integration of the gas dynamics equations requires a discretization of space, and the nodes at the boundaries of this discretization must satisfy the compressor equations. We modified the solution generated by an explicit algorithm to satisfy the compressor equations, while preserving the effect of the gas dynamics. This new solution is only modified at the boundaries and is obtained from solving a system of three differential equations and three algebraic equations. A Newton solver was used to solve this set of equations.

To test the system we simulated the configuration in Figure 3 following the schedule: the compressor was started at $t = 0.0$ s and the pipe had constant exterior temperature ($T_{ext} = 692^{o}$C) until $t = 1.0$ s. The external temperature profile shown in Figure 3 was used after $t = 1.0$ s. This was done to avoid flow reversal in the heat transfer loop due to the difference of temperature and pressure in the pipe sections. The system was simulated in this form until $t = 10$ s and produced the results in Figure 4. These plots show the density (ρ), the velocity of the fluid (u), the pressure (P) and the temperature (T). The plots show the intensive variables versus position in the pipe. Ten profiles of the system are shown each corresponding to one second of simulation, the lighter the shade of grey of the line, the earlier the time.

3.3.1 Novel simplification of the gas dynamics equations

The most accurate representation of gas dynamics in a pipe is achieved by using the Euler equations with a friction term (4-6). The information is propagated through the gas at different time scales. The time scales depend on the characteristics of the system, two of these characteristics are related to the speed of sound and the speed of the gas, and one characteristic is related only to the speed of the gas. The characteristics

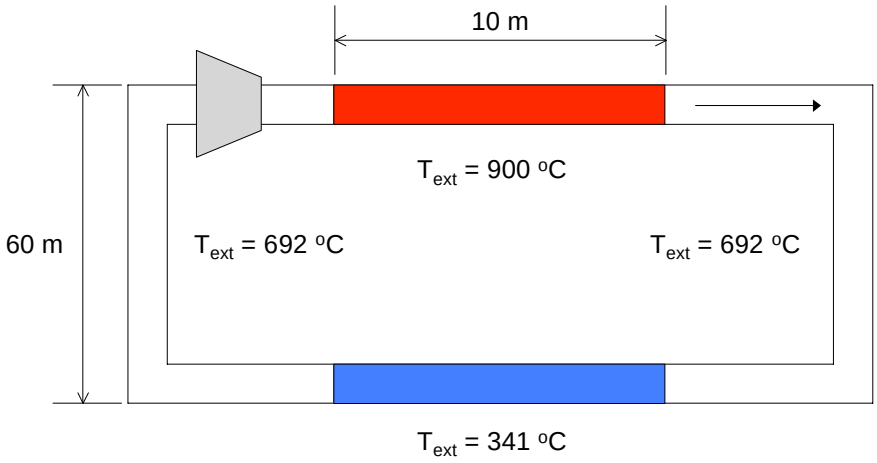

Figure 3: Simple heat transfer loop diagram.

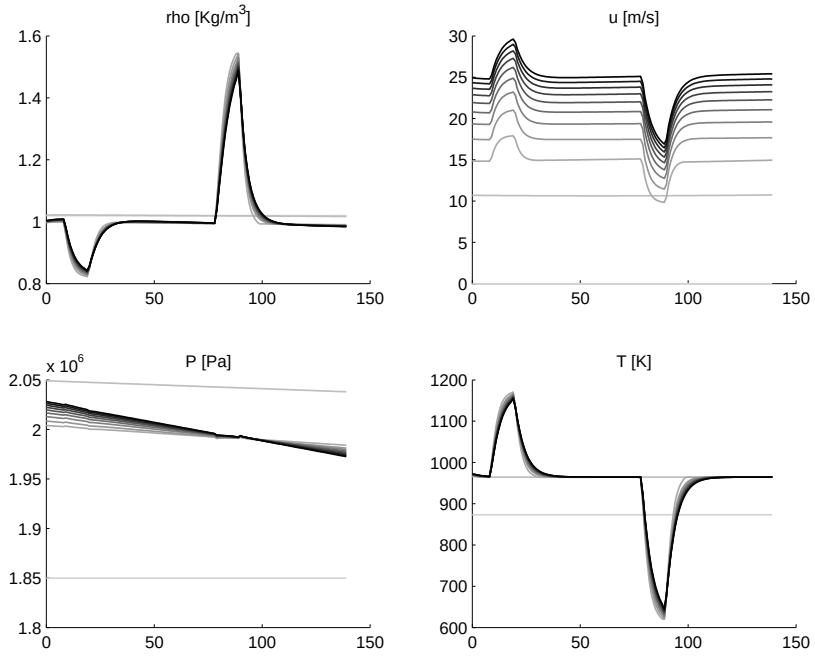

Figure 4: Intensive Variables along the loop, starting at the outlet of the compressor and finishing at the inlet.

related to the speed of sound are very fast and an accurate integration of the system requires the use of an explicit integrator with high-resolution methods. This kind of integrator was implemented for the examples of the previous section and their main drawback is their high CPU requirements. The time steps required for the explicit integration are very small and the simulations demand a high number of CPU cycles.

One way to avoid this complicated implementation is to simplify the equations taking into account only

the relevant time scales for the simulated phenomena. In this case, fast time scales are not necessary, because discrete disruptions in the flow of the gas are not expected. As changes in pressure propagate with the speed of sound, we can assume a quasi-equilibrium approximation for the equations related to the fast dynamics. These equations are the equations for mass conservation and momentum conservation. The simplified system is then:

- continuity

$$\frac{\partial(\rho v)}{\partial x} = 0, \tag{10}$$

- momentum

$$\frac{\partial P}{\partial x} = -\frac{2\rho f v|v|}{D}, \tag{11}$$

- energy

$$\frac{\partial \rho e}{\partial t} + \frac{\partial(\rho e v + P v)}{\partial x} = -\frac{4}{D_T} U(T - T_{ext}). \tag{12}$$

To validate the predictions from the new simplified system of equations, its result were compared with simulation results of the full system of equations. The experiment consisted of an open pipe where the inlet temperature, inlet pressure and the outlet pressure are set as boundary conditions. The inlet pressure is ramped over 12 s, until the pressure difference between the inlet and outlet pressure is 0.2 MPa. Figures 5 and 6 show the results, the gas profiles for the temperature, pressure, velocity and density.

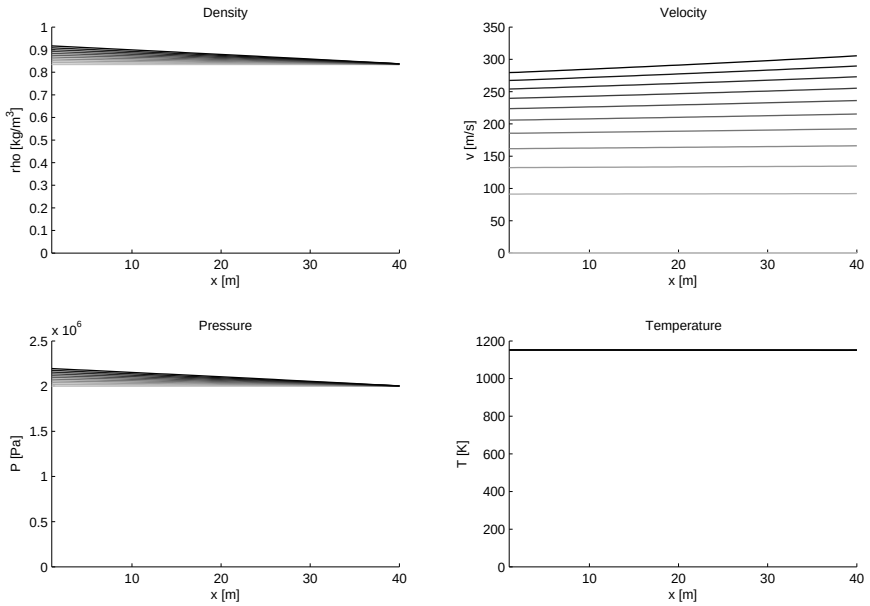

Figure 5: Simulation of pressure ramp in open pipe with the full system of equations and explicit integrator.

The results of the validation are satisfactory and show good agreement between the profiles obtained by the full system of equations (Figure 5) and the ones obtained by the simplified system of equations (Figure 6). The temperature profiles, pressure profiles and density profiles are similar and no major differences are observed. The velocity profiles produced by the full-system of equations show a delay compared to the velocity profiles produced by the simplified system of equations. This can be a explained by the nature of the

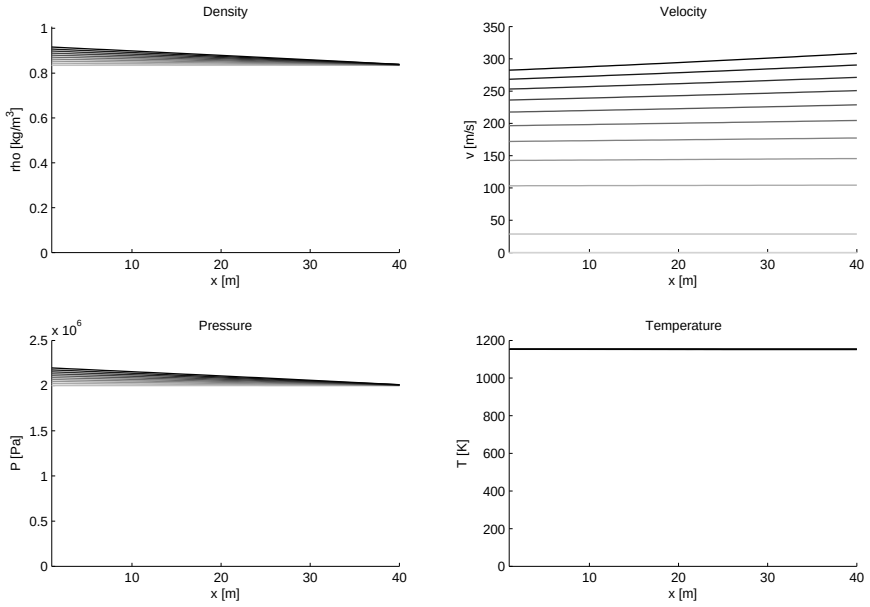

Figure 6: Simulation of pressure ramp in open pipe with the simplified system of equations and implicit integrator (JACOBIAN).

simplification; the simplified system of equations assumes that the changes in the gas due to compressibility effects take place instantaneously. On the other hand, the full system of equations takes some time to propagate these changes and that explains the delay (less than 1 s). The final steady-state is the same in both systems as it is expected.

3.3.2 Development and validation of a simplified model for the heat transfer loop

A model representing the dynamics of the heat transfer loop was created by using the simplification scheme from the previous section. This model represents the heat transfer from a heat source (gas from nuclear reactor) to a heat sink (an endothermic chemical process). The heat is transferred through the heat transfer loop and the system has the following parts: hot pipe, intermediate heat exchanger, heat transfer loop, compressor, process heat exchanger and cold pipe.

The system was designed using the specifications in the report written by C. B. Davis from INL [8]. This report used lumped models to design the system and it only calculated the steady state of the system at an optimal operation point. On the other hand, our system consisted of a distributed model with 1500 variables, which allowed to calculate the detailed transients and steady state for any configuration of the system.

The gas dynamics inside the loop were represented by using the simplified Navier-Stokes equations (Eqs. (10) – (12)). The compressor was described by using the compressor equations mentioned in the previous section (Eqs. (7) – (9)). The heat exchangers were represented by heat transfer equations that accounted for conduction of heat along the heat exchangers and for convection of heat from the gas. The equation representing these phenomena is:

$$V_{CV}\ Cp_{HX}\ \rho_{HX}\frac{\partial T_{HX}}{\partial t} = A_{CV}(\ k\frac{\partial^2 T_{HX}}{\partial x^2} + U_{hot}(T_{GasHot} - T_{HX}) + U_{cold}(T_{GasCold} - T_{HX})) \qquad (13)$$

The model was built by discretizing the spatial coordinate and it was validated using results from INL. The equations describing the flow of gas in a pipe and the heat exchangers were discretized in order to represent the variations along them. 50 nodes were used in the heat exchangers and 120 nodes were used in the pipe. The final model consisted of 1500 variables. This distributed model was validated by comparing its results to the results of the INL model at steady state [8]. The system followed a sequence of steps to achieve the same conditions of the INL model and the corresponding steady state. The results of both models are shown in Figure 7.

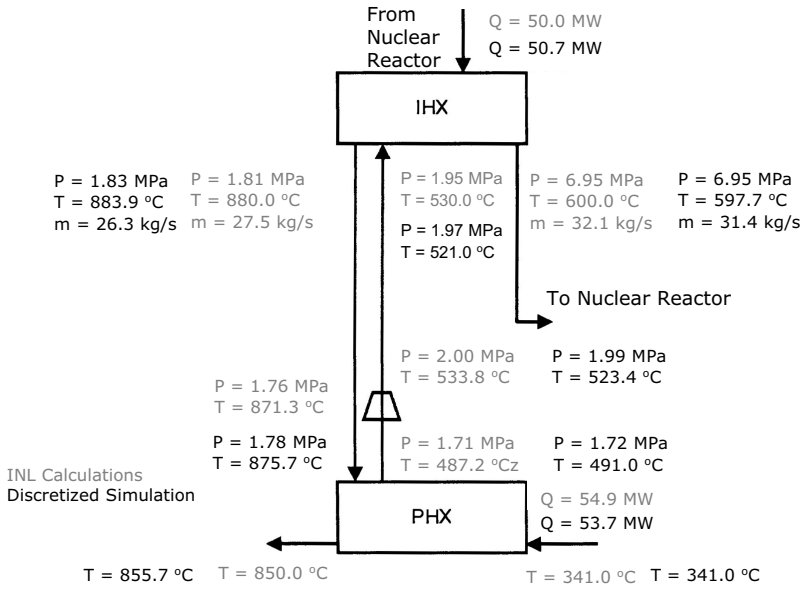

Figure 7: Comparison of results at steady state generated by INL and distributed model.

The new model allows us to look at variable profiles during transients. The plot in Figure 8 shows the transient profile of the helium density inside the loop. The final profile at time 1100 s corresponds to the steady state of the system at the operating point designed by INL. Different actions were executed to achieve this steady state; the first step was to start the compressor in the loop, to produce the necessary flow for heat transfer. Then the temperature in the hot pipe of the intermediate heat exchanger (IHX) was increased, mimicking an increase in the thermal power produced by the nuclear reactor. The final step was to boost the temperature and flow in the cold pipe of the process heat exchanger (PHX), mimicking the start-up of the chemical system for hydrogen production. The following sections explain this in more detail.

3.3.3 Validation of simplified system of equations representing the heat transfer loop using canonical form

As it was mentioned in the previous sections, it is necessary to show that the postulated simplification of the Euler equations eliminates the fast time scales of the system. The simplified system of equations is:

- continuity

$$\frac{\partial(\rho v)}{\partial x} = 0, \tag{14}$$

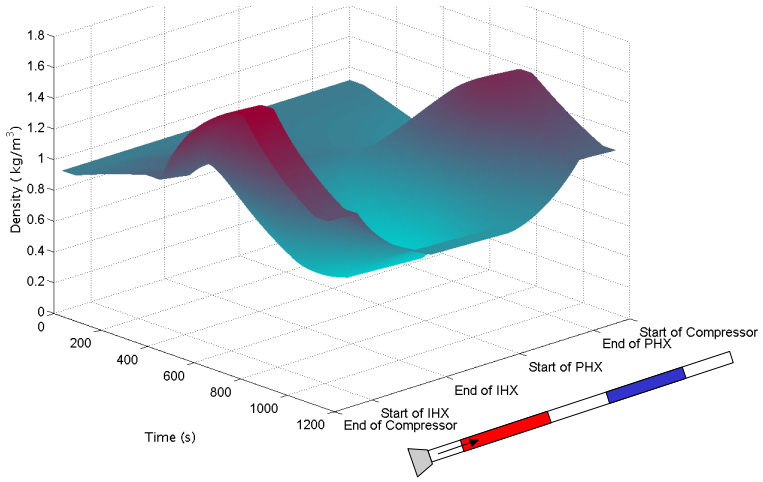

Figure 8: Transient profile of helium density inside the loop before achieving steady state at the operating point.

- momentum

$$\frac{\partial(P)}{\partial x} = -\frac{2\rho f v|v|}{D}, \tag{15}$$

- energy

$$\frac{\partial \rho e}{\partial t} + \frac{\partial(\rho h v + P v)}{\partial x} = -\frac{4}{D_T} U(T - T_{ext}). \tag{16}$$

An analysis of the system using the canonical form [28] was conducted to demonstrate that this simplification eliminates the fast time scales. To start we write the system in the form of:

$$\mathbf{M}(\mathbf{u})\mathbf{u}_t + \mathbf{F}'(\mathbf{u})\mathbf{u}_x = \mathbf{G}(\mathbf{u}(x,t)) \tag{17}$$

Where $\mathbf{u}$ corresponds to vector of the conserved variables of the system, $\mathbf{F}$ is the flux function and $\mathbf{F}'(\mathbf{u})$ is its Jacobian. Matrices $\mathbf{M}(\mathbf{u})$ and $\mathbf{F}'(\mathbf{u})$ can be transformed into the canonical form, because they form a regular matrix pencil. The corresponding regular matrices to transform the system are $\mathbf{P}$ and $\mathbf{Q}$, calculated according to [40]:

$$\mathbf{P} = \begin{bmatrix} -H & -\frac{\gamma u}{\gamma - 1} & 1 \\ 0 & \frac{1}{\gamma - 1} & 0 \\ 1 & -\frac{2}{\gamma - 1} & 0 \end{bmatrix}, \tag{18}$$

$$\mathbf{Q} = \begin{bmatrix} -\frac{1}{Hu} & 0 & 0 \\ 0 & 2 & 1 \\ 0 & 1 & 0 \end{bmatrix}. \tag{19}$$

Transforming the original system (17) by using $\mathbf{P}$ and $\mathbf{Q}$, we obtain the following system:

$$\overline{\mathbf{M}}(\mathbf{v})\mathbf{v}_t + \overline{\mathbf{F}}'(\mathbf{v})\mathbf{v}_x = \overline{\mathbf{G}}(\mathbf{v}(x,t)). \tag{20}$$

$\overline{\mathbf{M}}$, $\overline{\mathbf{F}'}$ and $\overline{\mathbf{G}}$ correspond to **PMQ**, **PF′Q** and **PGQ** in this representation. Then, the final form of the system is:

$$\begin{bmatrix} 0 & 1 & 0 \\ 0 & 0 & 0 \\ 0 & 0 & 0 \end{bmatrix} \mathbf{v}_t(x,t) + \begin{bmatrix} 1 & 0 & 0 \\ 0 & 1 & 0 \\ 0 & 0 & 1 \end{bmatrix} \mathbf{v}_x(x,t) = \overline{\mathbf{G}}(\mathbf{v}(x,t)). \tag{21}$$

The system (21) has the structure of a parabolic block, because the diagonal of matrix $\overline{\mathbf{M}}$ is null and the matrix $\overline{\mathbf{F}'}$ is the identity matrix. Being a parabolic block means the characteristic velocities of the system have been eliminated and it can be simulated using an implicit simulator such as JACOBIAN®.

3.3.4 Validation of simplified system of equations representing the heat transfer loop using RELAP

We have created a RELAP model of the intermediate heat transfer loop to validate the simulations of the simplified systems of equations (Eqs. (14), (15) and (16)). Based on the work of Cliff Davis [8] from INL, we constructed a model with the structure of Figure 9. At this point in time, the steady-state simulation results of the JACOBIAN® and RELAP are being compared. The next step is to compare the transient response of each model.

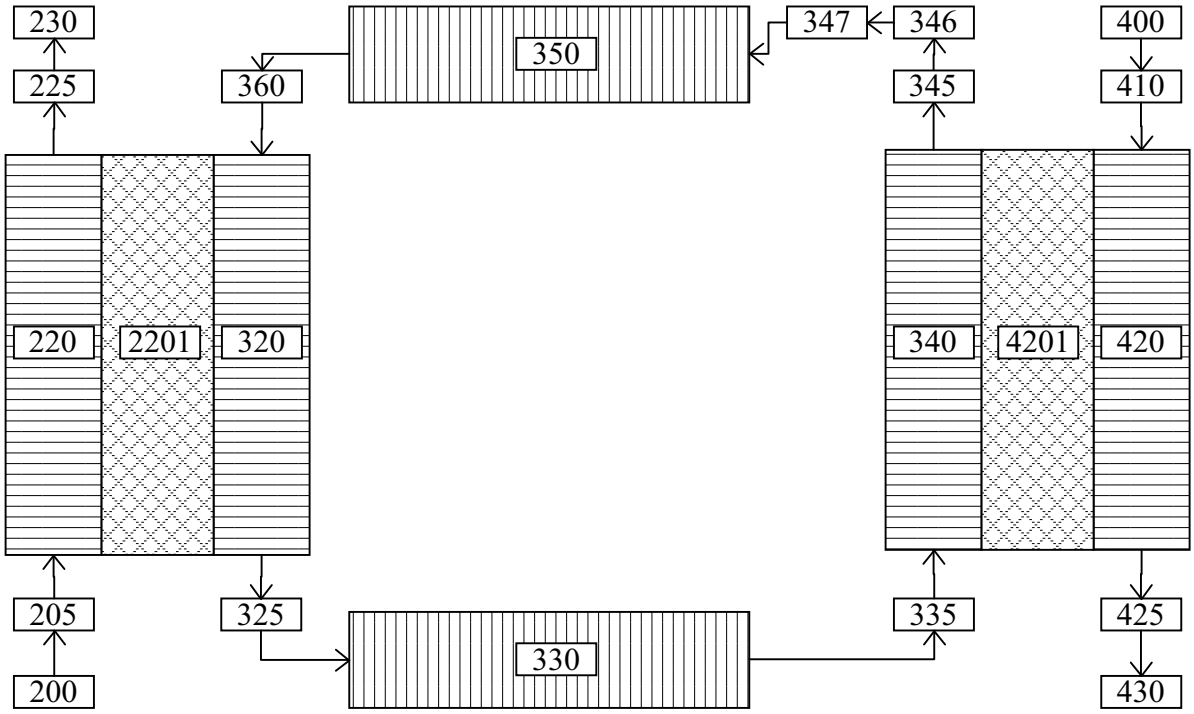

Figure 9: RELAP Model.

We created a model of the heat transfer loop in JACOBIAN and in RELAP. These models have the same parameters for heat transfer, helium properties, compressor, etc. We simulated the steady state of both models. This steady state has a flow of gas of 27kg/s. The temperature in the loop reaches 880 C. This loop transfers 54 MW of thermal energy to the steam in the process heat exchanger. The following plots show the temperature and pressure profiles of helium inside the loop. The plots are shown in an arbitrary scale

to show the detail in each section. Each section of the plots is scaled to ten arbitrary length units, in order to show the details of the profile for each section. Table 1 explains this.

Table 1: Loop description.

Adjusted relative distance from compressor	**Section**	**Actual length**
1 - 10	Cold leg	90m
11 - 20	Intermediate heat exchanger	8.8m
21 - 30	Hot leg	90m
31 - 40	Process heat exchanger	10m

Figures 10 and 11 show the temperature and pressure profiles inside loop along the different units. The profiles where calculated using JACOBIAN® and they were validated using RELAP5. The profiles so generated show good agreement and our JACOBIAN model is able to capture the steady state of the model at the operation point.

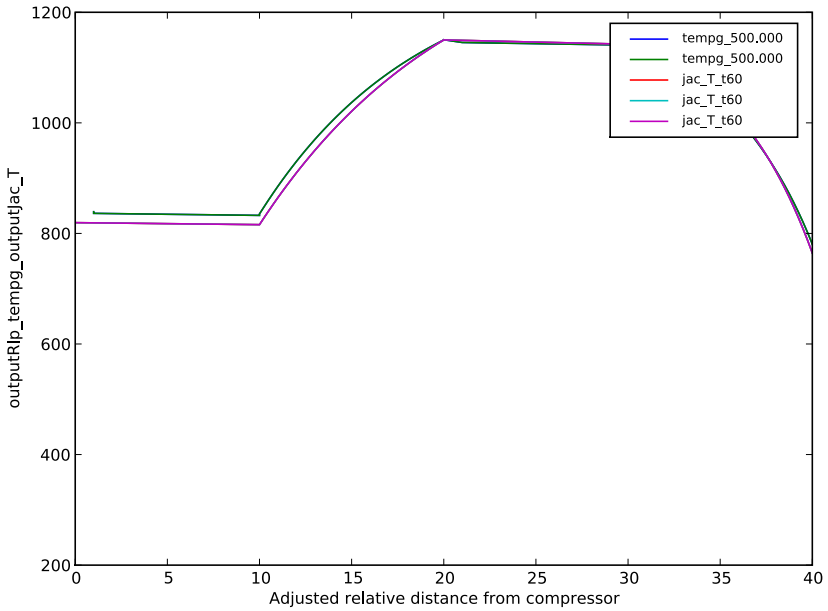

Figure 10: Temperature profile in the loop (arbitrary scale to show the effects in each section).

3.3.5 Validation of the dynamics

The next step was to validate the dynamics of the model built using changes in the input variables. The starting point was the operating steady state shown in the previous section, and two different modifications were implemented and analyzed. The first modification was to increase the temperature of the steam going into the process heat exchanger. The second modification was to decrease the flow of gas inside the loop by decreasing the power of the pump. Figures 12 and 13 show how the pressure and temperature inside the loop increase after increasing the temperature of the steam going into the process heat exchanger by 100K. The models compared are implemented in RELAP and in JACOBIAN. RELAP represents the gas dynamics using a semi-implicit method and JACOBIAN uses an implicit method with a simplified version of the inviscid Navier-Stokes equations. The change in temperature takes 60s and it was implemented as a linear ramp. Both figures show the initial steady state and the final state after 500s.

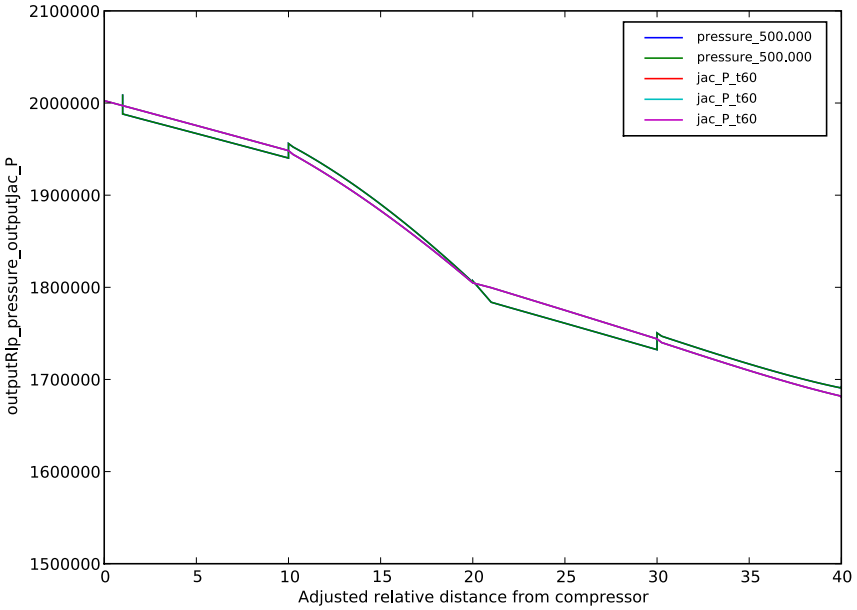

Figure 11: Pressure profile in the loop (arbitrary scale to show the effects in each section).

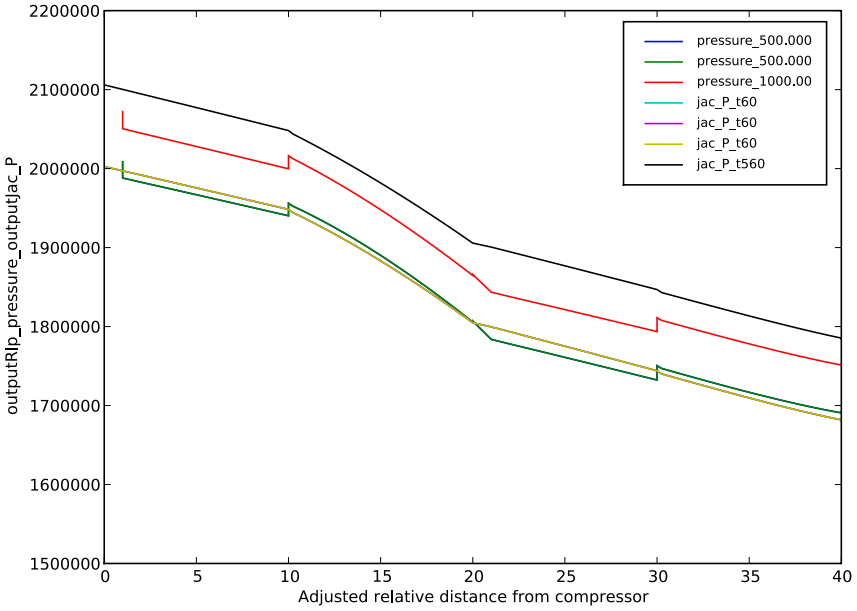

Figure 12: Pressure profiles before and after increasing inlet steam temperature to PHX.

The figure shows that the final pressure in the JACOBIAN model is, on average, 0.4MPa higher than the pressure in the profile generated by RELAP. The reason for this is the loss of mass inside the loop in the RELAP model, produced by an error in the numerical solution of the system. Figure 14 shows how the total mass of gas inside the loop changes during the transient simulation. The change in mass in the order of 2% which is also the difference in the final pressure of the system in the JACOBIAN and RELAP models. The difference in the temperature profile is less significant.

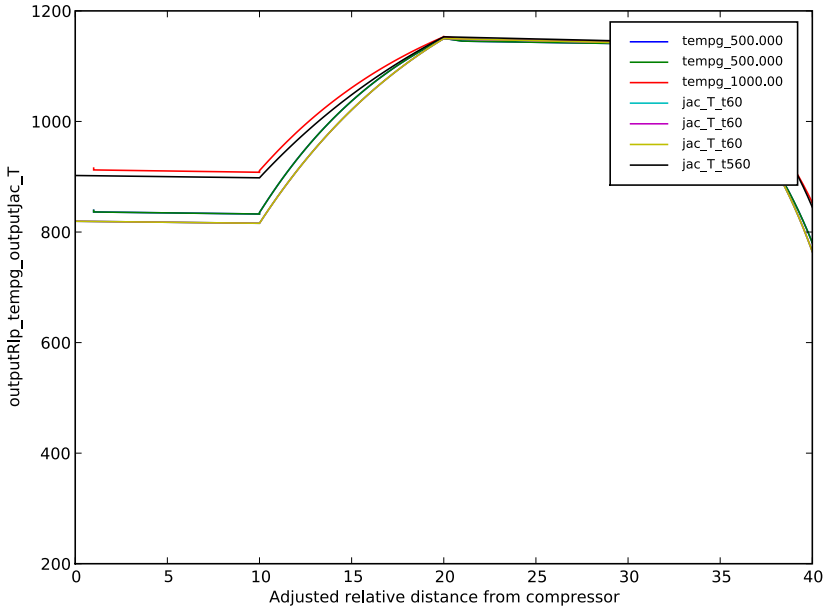

Figure 13: Temperature profiles before and after increasing inlet steam temperature to PHX.

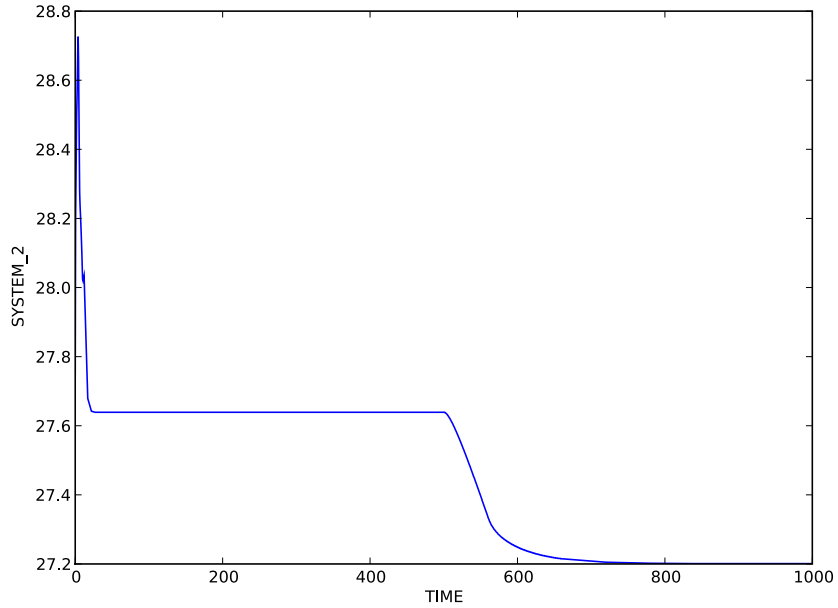

Figure 14: Evolution of helium mass inside the loop after increasing inlet steam temperature to PHX.

A second scenario shows how the profiles inside the loop change when the flow at the pump is decreased by 10%. As in the previous situation, the pressure profiles produced by JACOBIAN and RELAP are similar at the initial steady state (Figure 15). However, the pressure profiles differ at the final steady state; this time the difference is in the order of .015 MPa. The decrease of the helium mass inside the loop explains again the situation (Figure 17). The difference in the temperature profile is not significant (Figure 16).

The second step was to compare the dynamics of the JACOBIAN and RELAP models. The results

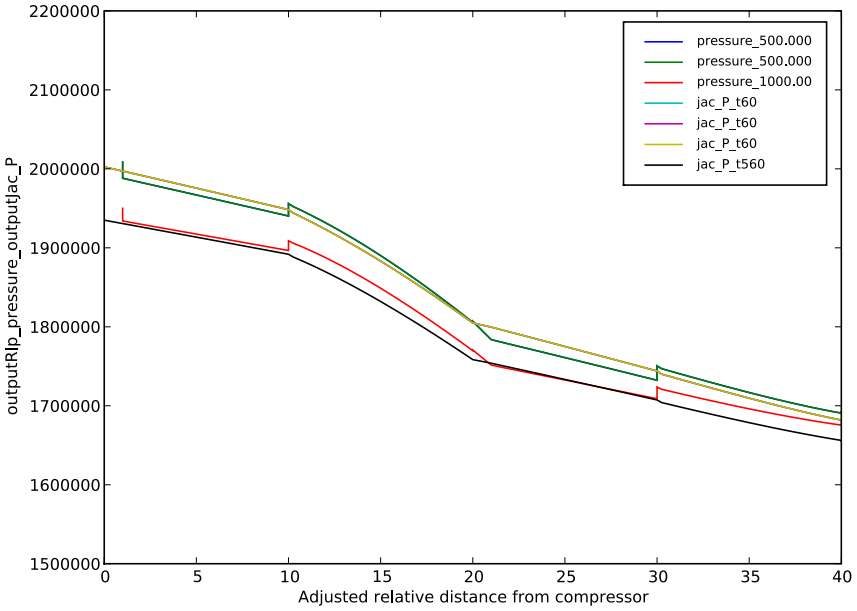

Figure 15: Pressure profiles before and after decrease in loop pump power.

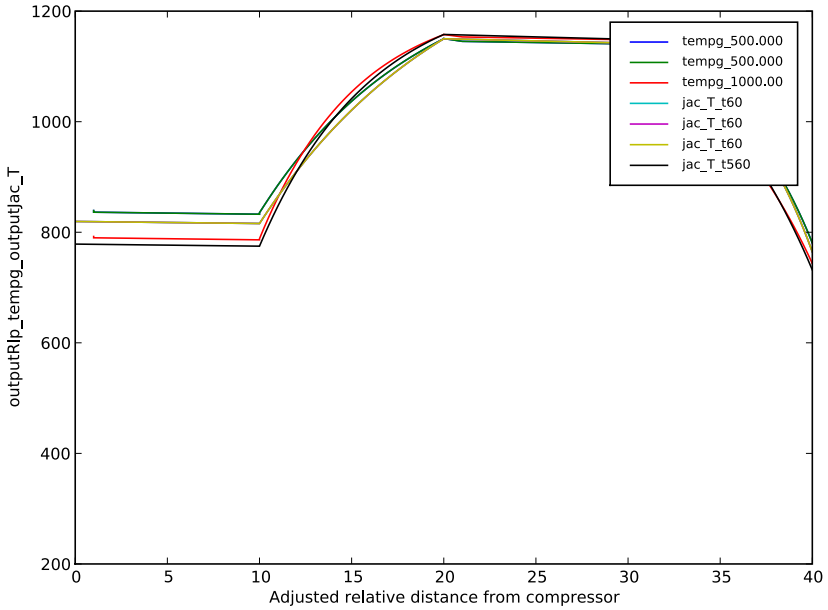

Figure 16: Temperature profiles before and after decrease in loop pump power.

show that the JACOBIAN model represent similar time scales as the RELAP model. The dynamics of both models is compared at different points inside the loop. The state variables were normalized for comparison, because the mass error in RELAP changed the range. Both models show good agreement. Figures 19 and 18 show the temperature and pressure inside the loop at the end of the process heat exchanger. Figures 21 and 20 show what happens at the start of the intermediate heat exchanger and Figures 23 and 22 show the response at the end of this heat exchanger. The profiles are in very good agreement and the times scales in RELAP and JACOBIAN are very similar. Only Figure 23 shows that JACOBIAN responds 15s faster than

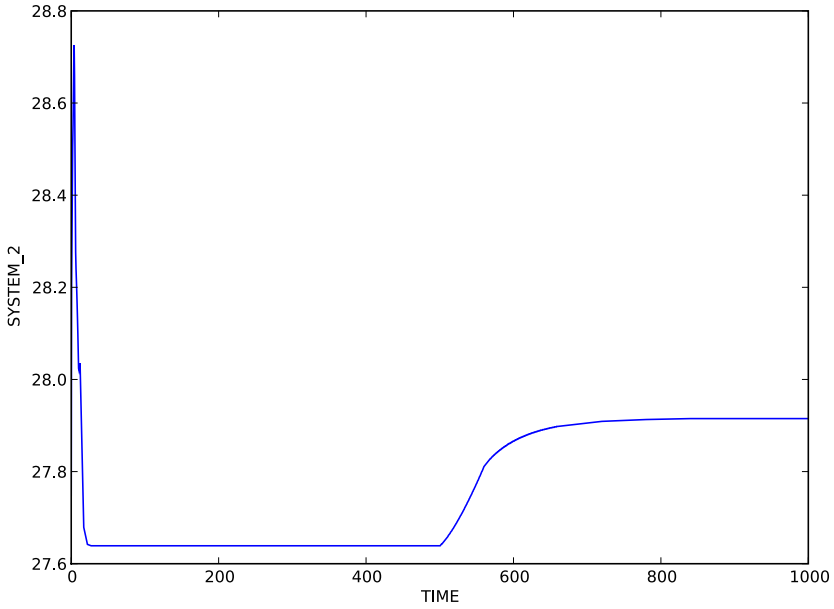

Figure 17: Evolution of helium mass inside the loop after decrease in loop pump power.

RELAP, which is a small difference.

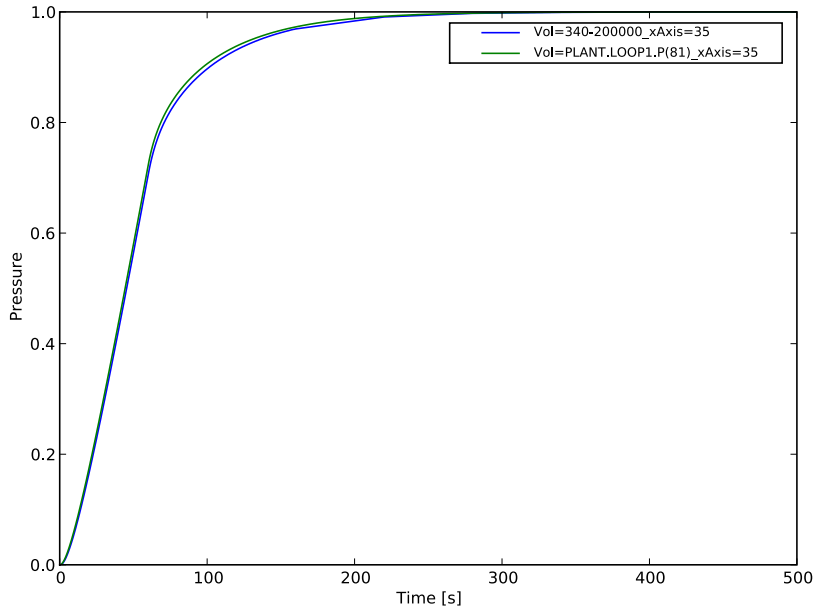

Figure 18: Scaled pressure inside the loop at the end of the PHX.

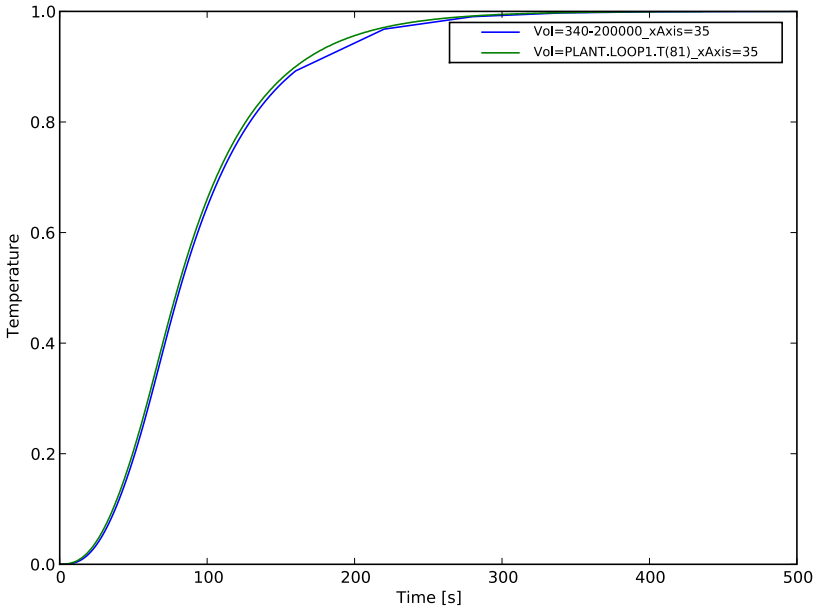

Figure 19: Scaled temperature inside the loop at the end of the PHX.

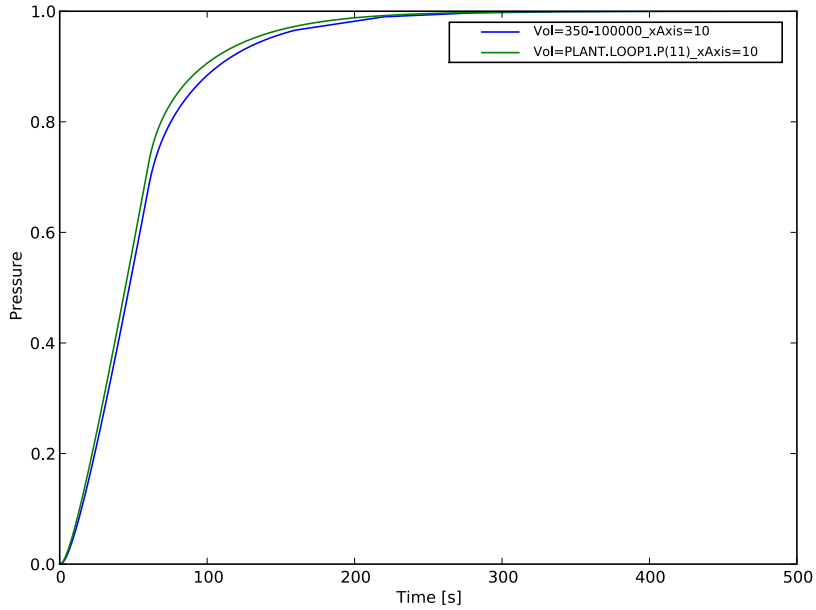

Figure 20: Scaled pressure inside the loop at the start of the IHX.

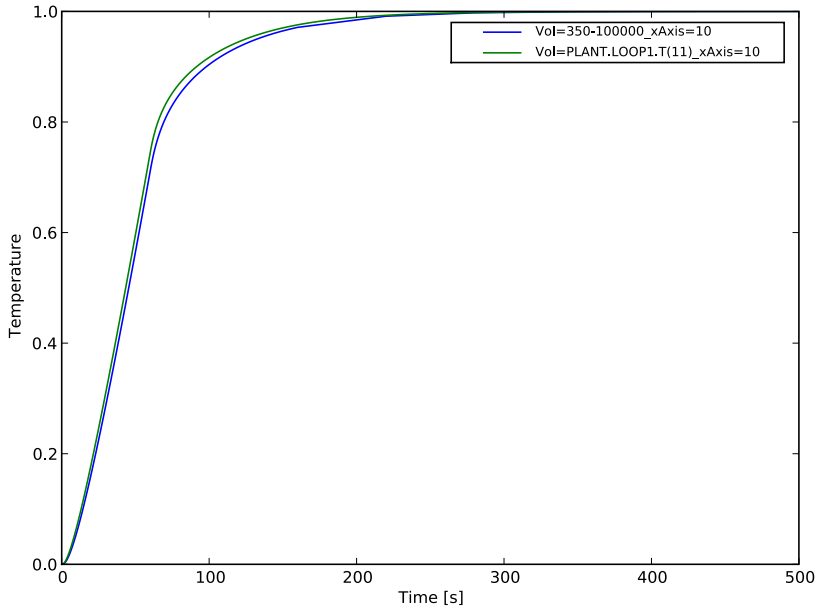

Figure 21: Scaled temperature inside the loop at the start of IHX.

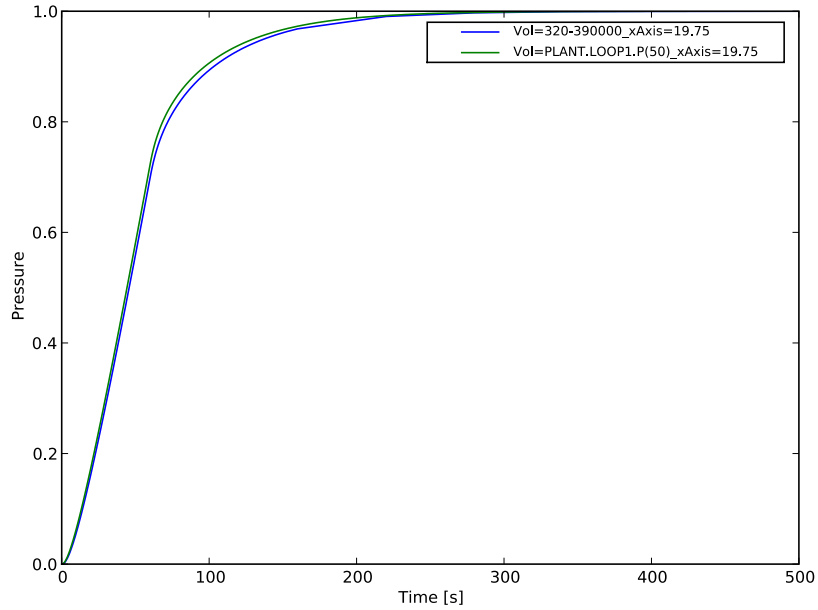

Figure 22: Scaled pressure inside the loop at the end of the IHX.

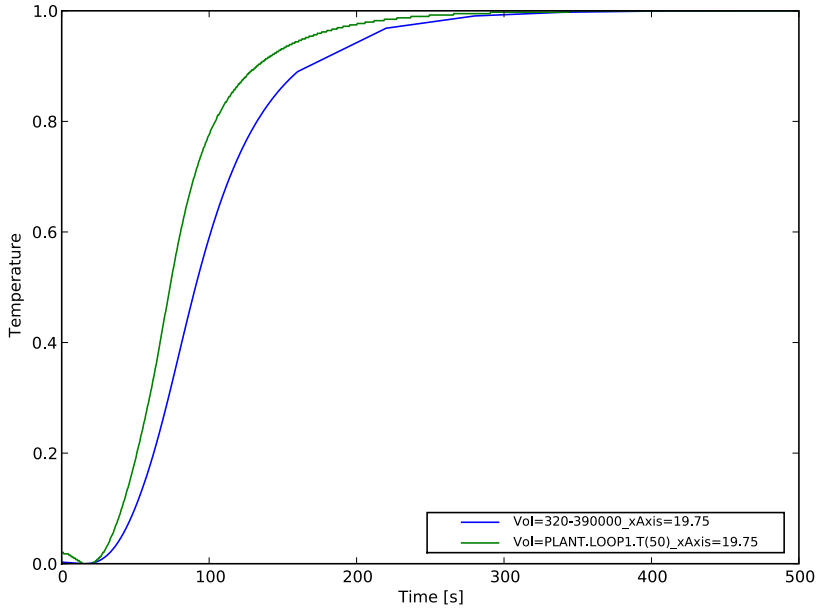

Figure 23: Scaled temperature inside the loop at the end of the IHX.

3.4 Implementation of nuclear reactor model to build a two-loop system

The next step in this project was to implement a nuclear reactor model as heat source for the system. Figure 24 shows the desired configuration. This configuration will allow to study the effects of transients on the nuclear reactor.

A model for the nuclear reactor developed by Chunyun Wang at MIT [45] was adapted and incorporated into the heat transfer system detailed in the previous section. This model was based on a pebble bed modular reactor (PBMR) as the one in Figure 25 and it used helium as coolant. The model used the discretization in Figure 25 to represent the core. The core has radial symmetry and the discretization took advantage of it by using a two-dimensional discretization considering the radial and the vertical coordinates.

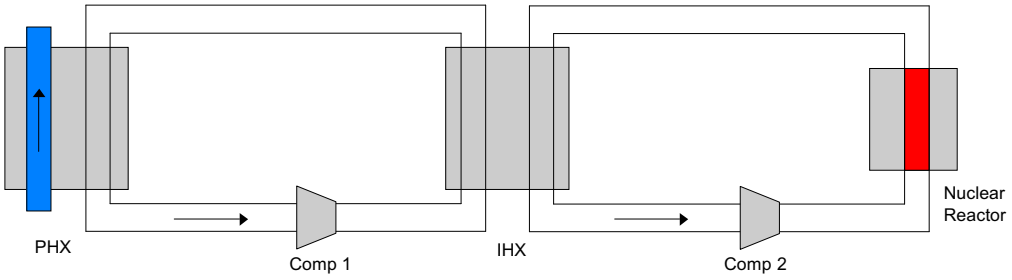

Figure 24: Heat transfer system with two loops.

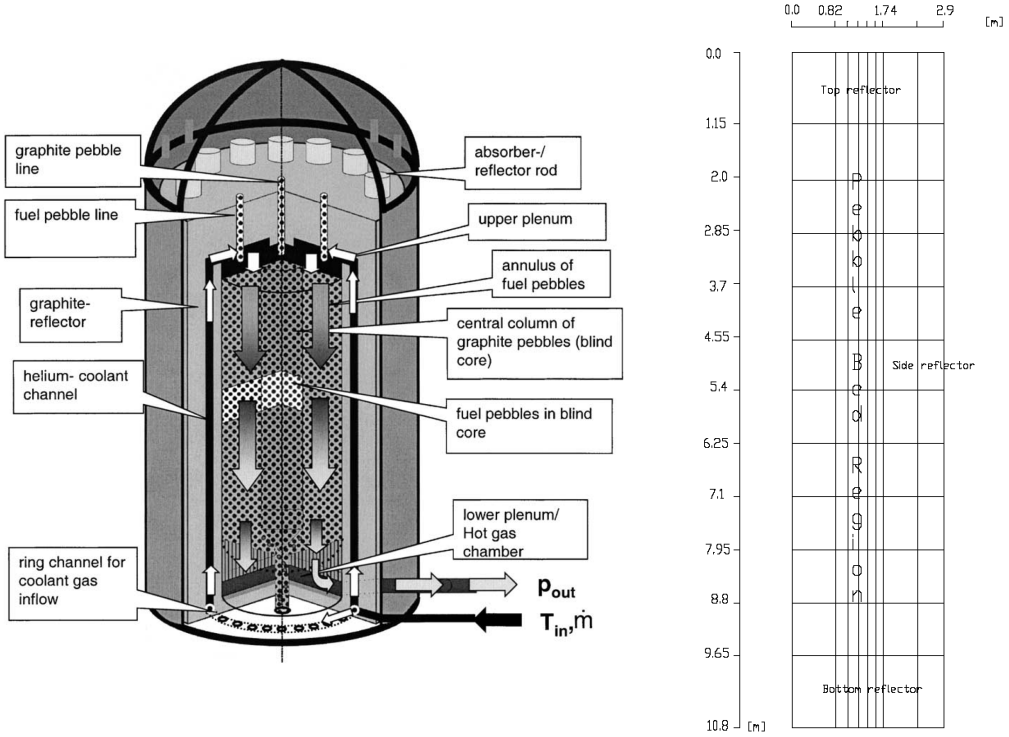

Figure 25: Pebble bed nuclear reactor and core discretization.

This model was a collection of submodels and it was successfully implemented in JACOBIAN. The

submodels represented the phenomena happening inside the core: convective heat transfer between the core and the helium; conductive and radiative heat transfer in the core and reflectors; reactivity as a function of temperature, control rods and poison; and fission power generated (point kinetics).

The model was simulated in JACOBIAN and Figure 26 shows the steady-state temperature profile of the helium inside the core. Figure 27 shows the steady-state temperature profile of the pebbles and the reflectors in the core. The average temperature of the helium coming out of the reactor is 907°C. The average temperature in the core is 930°C and the maximum temperature in the core is 1235°C.

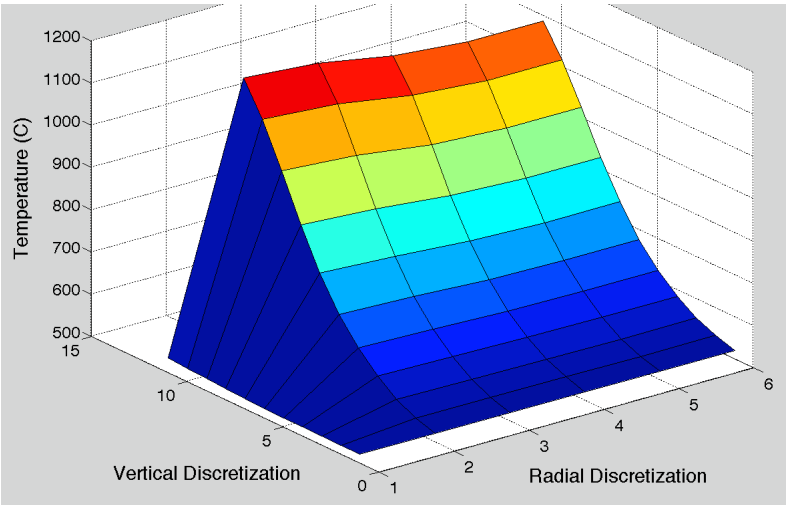

Figure 26: Temperature of helium passing through the core.

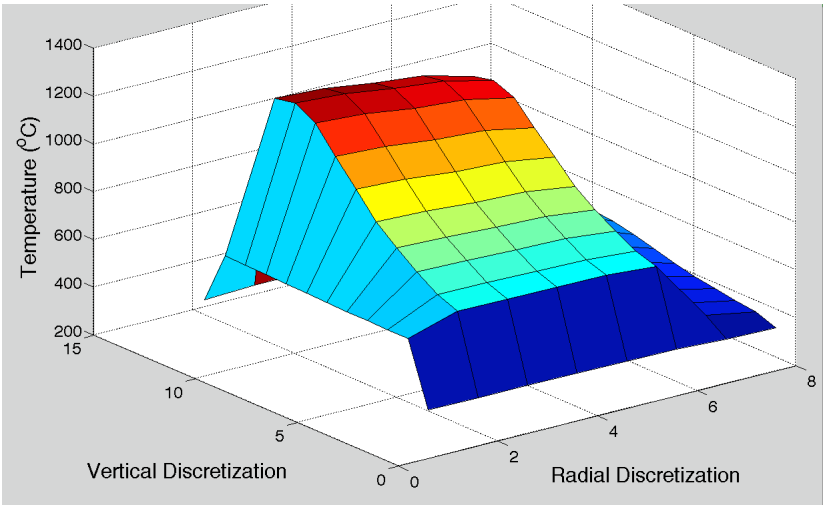

Figure 27: Temperature of pebbles and reflectors in the core.

3.4.1 Simulation of Start-Up of the Two-Loop System

A simple start-up schedule was simulated as a test for the two-loop system model created in the previous section. The start-up schedule had four stages (Table 2), and the first one was to stabilize the system at a low power level. This was achieved by running the compressors and nuclear reactor at 1% of the designed power level and waiting until the system reached a steady state. Second, the heat removal system was started by increasing the power of the compressors in both loops, and by increasing the flow of gas on the cold side of PHX. Third, the heat generated in the nuclear reactor was boosted until it reached the design point. Finally, the temperature in the cold side of the PHX was raised, representing the start-up of the chemical plant.

Table 2: Start-up schedule

Stage	**Event**	**Time**
Stabilization	Compressors running at 1%	0 s
Start heat removal	Increase power on compressor in Loop 1	300 s
	Increase pressure on cold side of PHX	
	Increase power on compressor in Loop 2	660 s
Increase heat	Add rod reactivity until QFission = 200 MW	986 s
Connection to chemical plant	Increase temperature in the cold side of PHX	6127 s

Figure 28 shows the temperature of helium at different points in the system. The first point (blue) is at the start of the PHX, and the second point (red) is at the start of the IHX. The third point is at the outlet of the nuclear reactor. The helium temperature at the start of the PHX and at the outlet of the nuclear reactor have a similar profile after 1500 s. However, these profiles differ before 1500 s, this difference can be explained by the thermal transients generated by the thermal inertia of the IHX. On the other hand, the start of the IHX (red) is one of the coldest along the loop. These profiles show the temperature gradients transferring the heat from the nuclear reactor to the chemical plant.

Figure 29 displays the temperature of different materials in the system. The first point (red) is the temperature of the metal in the middle of the IHX. The second point (green) and the third point (blue) are the maximum and the average temperature of the pebbles inside the nuclear reactor. The temperature in the IHX has, after 1500 s, a similar profile to the helium temperature at the outlet of the nuclear reactor. However, these profiles are very different before 1500 s, and this can be explained again by the thermal inertia of the heat exchangers.

Figure 29 also shows the large difference between the maximum and the average temperature in the nuclear reactor, this difference is 317°C. This shows the importance of using a distributed model for the nuclear reactor core; we are worried about the maximum temperature that can be reached inside the core and not just the average temperature. The sections with very high temperature are the ones that have to be carefully monitored.

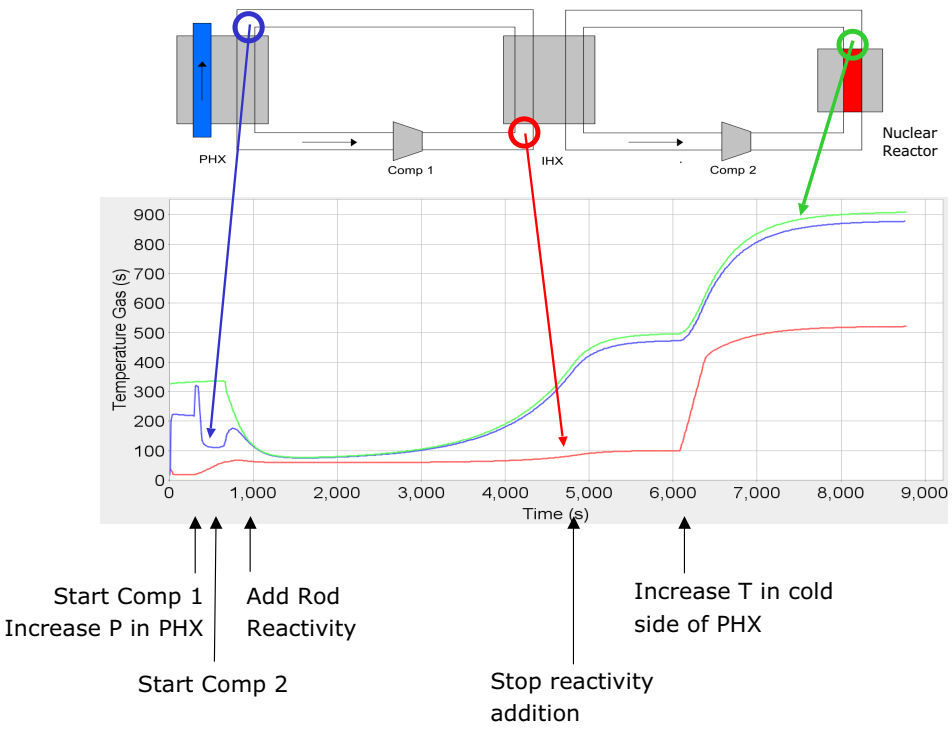

Figure 28: Temperature of helium at different points in the system.

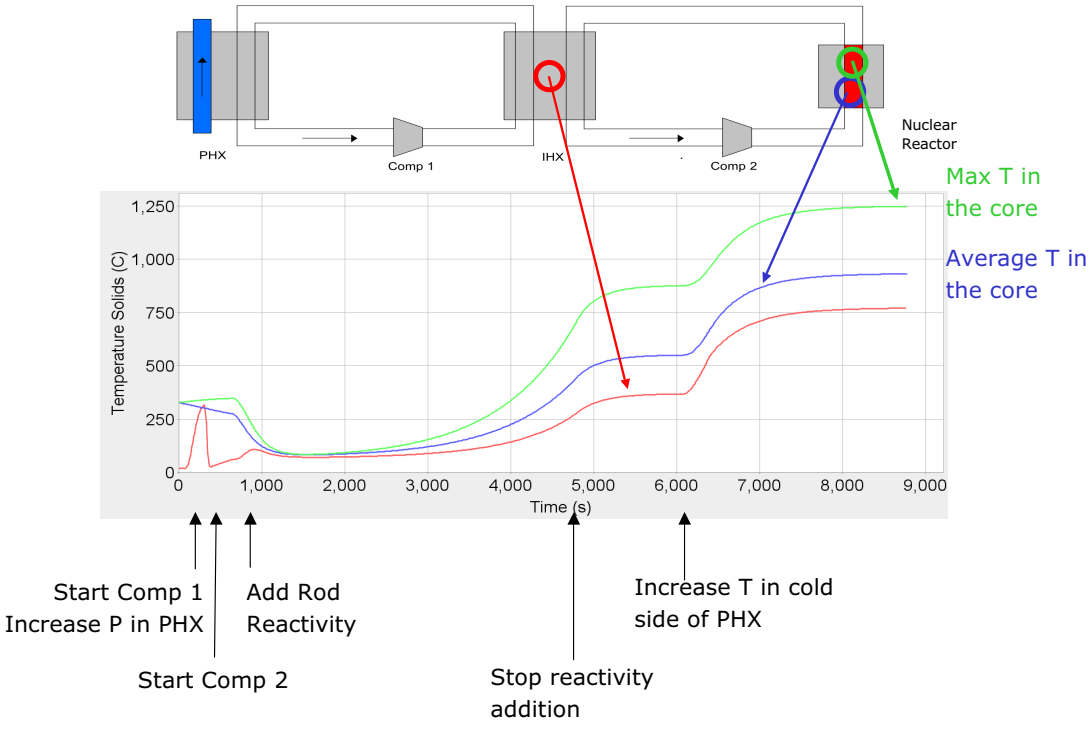

Figure 29: Temperature of pebbles in the core and metal in heat exchanger.

4 Task 2: Modeling of the Sulfur-Iodine thermochemical cycle

Thermochemical water splitting is considered as an energy-efficient, low-cost process for hydrogen production. Among the large-scale, cost-effective and environmentally-attractive hydrogen production processes, the Sulfur-Iodine (SI) thermochemical cycle appears to be one of the most promising. In this cycle, iodine and sulfur dioxide are combined with water, forming hydrogen iodide and sulfuric acid, which are immiscible and can be readily separated. Then, the sulfuric acid is decomposed at about 850°C releasing the oxygen and recycling the sulfur-dioxide. Finally, the hydrogen iodide is decomposed at about 400°C, releasing the hydrogen and recycling the iodine. A sketch of the integrated SI thermochemical cycle is presented in Figure 30

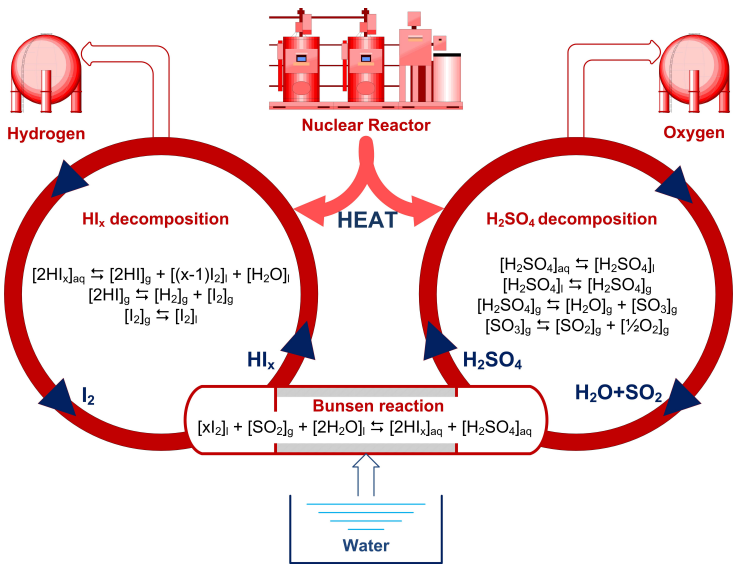

Figure 30: Reactions occurring in the SI Thermochemical Cycle.

General Atomics [5] suggests the flowsheet shown in Figure 31. According to this flowsheet the SI cycle can be split into three sections:

- Recycle Acids Generation (Section I):

$$[xI_2]_l + [SO_2]_g + [2H_2O]_l \leftrightharpoons [2HI_x]_{aq} + [H_2SO_4]_{aq}$$

  This reaction, named the Bunsen reaction, proceeds exothermically in the liquid phase and produces two immiscible aqueous acid phases, with the dense phase containing HI_x and the light phase containing H_2SO_4. This phase split is the key to the cycle's success, but the resulting liquid-liquid equilibrium (LLE) is difficult to model.

- Sulfuric Acid Concentration and Decomposition (Section II):

$$\begin{aligned}
[H_2SO_4]_{aq} &\leftrightharpoons [H_2SO_4]_l \\
[H_2SO_4]_l &\leftrightharpoons [H_2SO_4]_g \\
[H_2SO_4]_g &\leftrightharpoons [H_2O]_g + [SO_3]_g \\
[SO_3]_g &\leftrightharpoons [SO_2]_g + [1/2O_2]_g
\end{aligned}$$

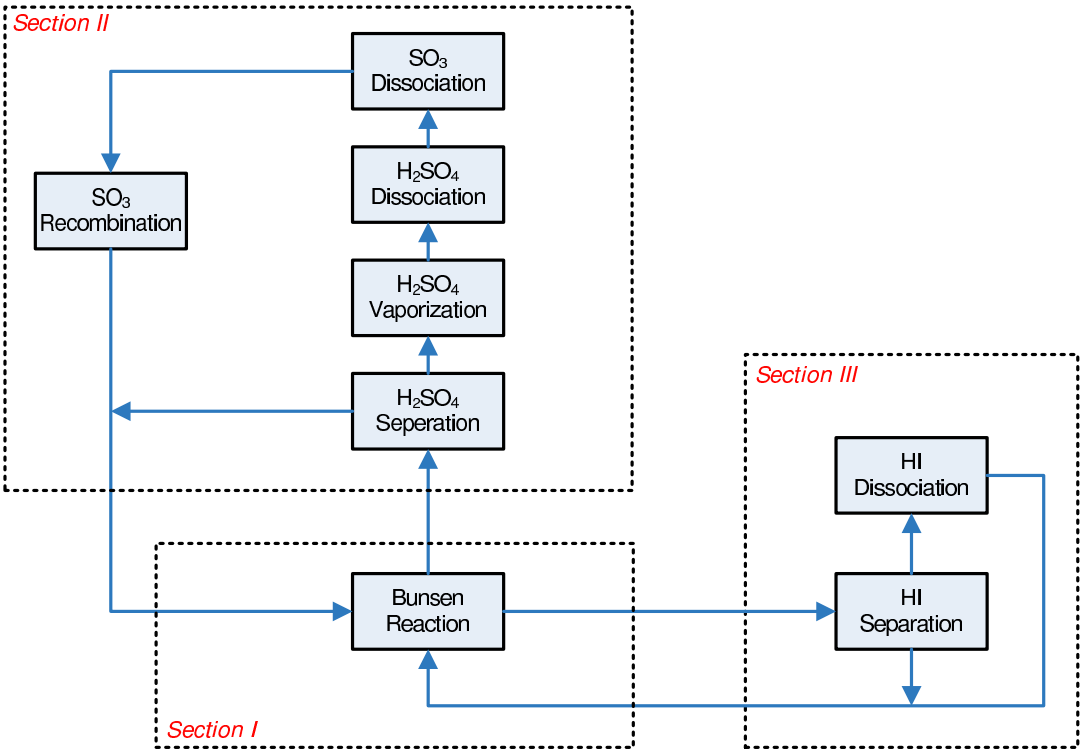

Figure 31: Operational Sections of the SI Thermochemical Cycle.

Experience from the sulfuric acid industry can be applied for the simulation of this section. Modeling uncertainty arises from the high temperatures of this section and the complex formation of H_2SO_4 and H_2O at high temperatures and/or concentrations.

- HI Concentration and Decomposition (Section III):

$$[2HI_x]_{aq} \leftrightharpoons [2HI]_g + [(x-1)I_2]_l + [H_2O]_l$$
$$[2HI]_g \leftrightharpoons [H_2]_g + [I_2]_g$$
$$[I_2]_g \leftrightharpoons [I_2]_l$$

The main difficulties that have to be overcome in this section include the extraction of HI from the HI_x mixture because of the presence of an azeotrope in the mixture, the possibility of iodine precipitating as a solid ($T_m = 113.6°C$) and the strong immiscibility of the H_2O-HI-I_2 mixture.

It is evident from the above that a major challenge in simulating the SI process is modeling of the chemical equlibria in the major unit operations. In particular, special attention has to be paid to predicting the equlibria of the electrolytes' partial dissociation and the stable phase split. A significant bottleneck in the modeling of this process is the empirical nature of the existing models for multi-electrolyte solutions and their restricted validity (low temperatures and pressures). The model applied for the calculation of the chemical equilibria has to be valid for temperatures up to 800°C. Furthermore, the prediction of speciation in the process sections, which is not among the traditional virtues of electrolyte thermodynamic models, is important for the simulation of thermochemical cycles. Hence, our research efforts focused on the development of thermodynamic models for the solutions of interest at the conditions in question and advanced optimization techniques for parameter estimation in phase equilibrium problems and thermodynamic data reduction.

4.1 Thermodynamic models used in the literature for the simulation of the Sulfur-Iodine Thermochemical Cycle

The thermodynamics of the SI thermochemical cycle are very complex, because they involve multiple vapor-liquid-solid equilibria in solutions with multiple electrolytes and solvents and at very high temperatures. One very important observation that came from analysing the aqueous sulfuric acid solution at ambient conditions is that, although the existing models are capable of describing the vapor-liquid equilibrium, they are deficient in the prediction of the system speciation. It was considered imperative to re-examine the accuracy of the available models and it is noteworthy that measurements of the speciation in the various stages of the sulfur-iodine thermochemical cycle will be needed for the validation of the models. It should be noted that the accurate prediction of the speciation is of great importance for the thermochemical cycles, because the main interest is in the prediction of the products of the reactions. In order to explore the latter the various models that are applied for the simulation of the stages of the SI cycle were examined with the (little) available experimental data. The models that are used in the efforts simulating the SI process can be categorized as follows:

- Neumann-Engels model (ProSim Software, CEA France):
  The model developed by Neumann (and its similar version developed by Engels and Knoche [9]) are based on the concept of hydration. The thermodynamics of the hydrogen iodine (Ref. [9]) and sulfuric acid (Ref. [4]) systems are represented on the basis of the assumption that the acids dissociate in water and are solvated (hydrated) resulting to neutral species. The advantage of this approach is that simple models, such as the NRTL model or the TK Wilson model, can be applied, without having to deal with the ionic effects. However, the resulting picture is an unrealistic description of the solution (the acids are expected to be hydrated, but it is unreasonable to consider that they become neutral). Furthermore, at infinite dilution there are conflicts with the Debye-Hückel law. Nonetheless, this model is able to capture the VLE behavior of the system, but in terms of predicting the speciation of the system it is deficient. Figures 32 and 33 show the application of the Engels-Knoche Wilson model and the Bosen-Engels NRTL model to represent the VLE of the hydrogen iodine and sulfuric acid systems. Using the available NMR measurements of the speciation of the sulfuric acid system and the model of Engels it is evident that the prediction is very poor. Although, detailed spectra measurements are not available for the HI-H_2O system it should be pointed out that hydrogen iodide is considered to be the strongest acid, hence the dissociation profile shown in Figure 32 seems unrealistic.

- Mathias model (ASPENOne Software, GA USA):
  Mathias [29] has developed a model that utilizes the electrolyte-NRTL model and the concepts of hydration and ions-water complex formation. This picture is a much more realistic description of the system. According to General Atomics [5] the model is able to capture they main characteristics of the process. However, problems have been reported with the estimated values for the I_2 dielectric constant. Although measurements of the speciation for the HI-H_2 system are not available, the model predictions for the HI system at the left side of the azeotrope appear reasonable (Figure 34). However, application of the sulfuric acid model to ambient conditions shows again a poor predictive capability of the speciation (Figure 35). Furthermore, the use of the original data of Gmitro and Vermeulen [12] for fitting the H_2SO_4 model (and not the revised values that are available in the latest editions of Perry's Chemical Engineers' Handbook) results in relatively deficient predictions of the azeotrope. It should be pointed out that, when the equilibrium of the acid dissociation is fitted using only activity-type measurements, the prediction of speciation can be very poor. This issue gives rise to the necessity of acquiring more experimental data for the systems of interest.

- UNIQUAC model (OLI Software, JAEA Japan):
  We did not have the chance to work with the version of the UNIQUAC model of OLI. According to Dr. Hiroyuki Sato from JAEA the model is continuously updated with experimental data from the bench-scale SI plants that operate in JAEA, but they have problems integrating the OLI Software with

their main simulation engine.

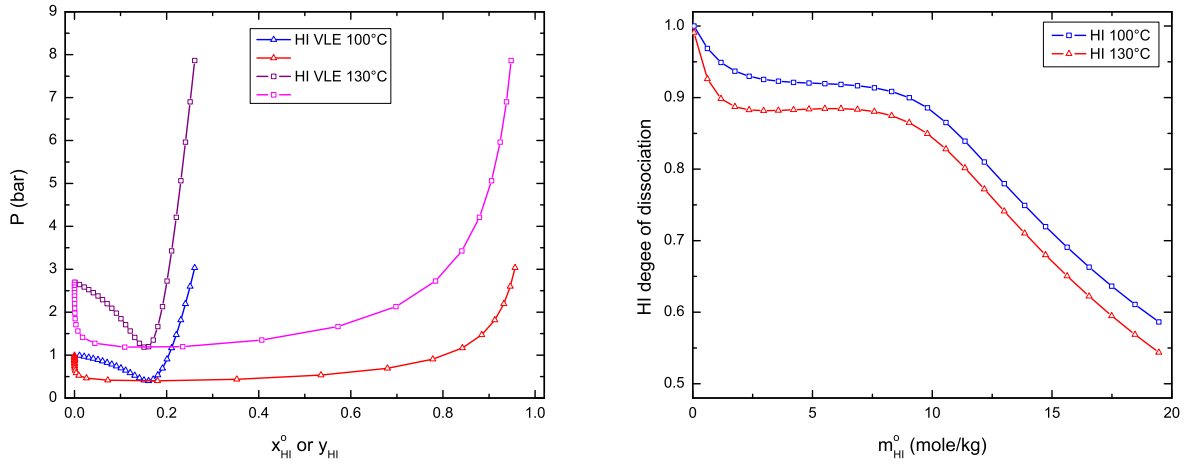

Figure 32: Vapor – liquid equilibrium and degree of acid dissociation for the system HI-H_2O using Engels-Knoche [9] model.

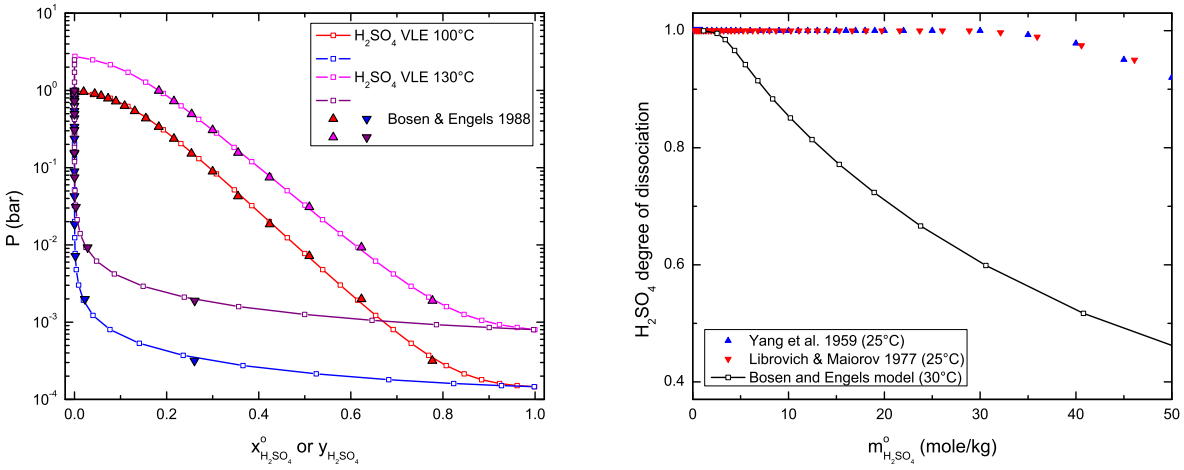

Figure 33: Vapor – liquid equilibrium and degree of acid dissociation for the system H_2SO_4-H_2O using Bosen-Engels [4] model.

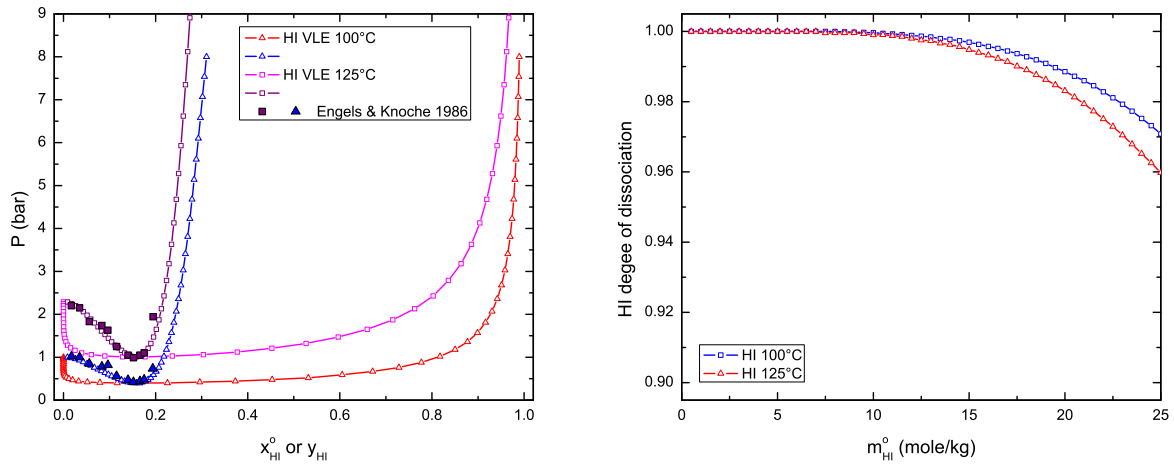

Figure 34: Vapor – liquid equilibrium and degree of acid dissociation for the system HI-H_2O using Mathias (AspenOne) model [29, 5].

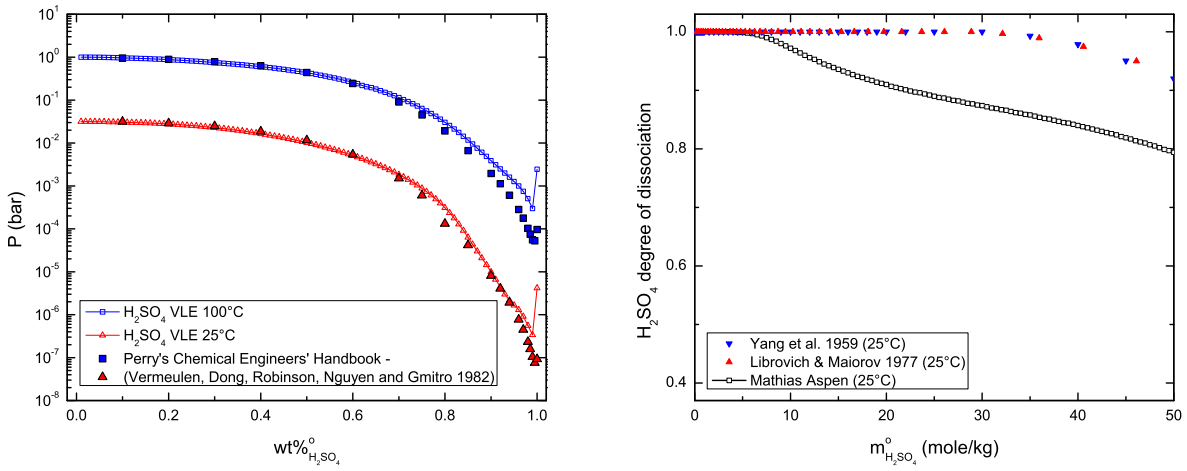

Figure 35: Vapor – liquid equilibrium and degree of acid dissociation for the system H_2SO_4-H_2O using Mathias (AspenOne) model [29, 5].

4.2 Refined electrolyte-NRTL model

The model chosen for the simulation of the thermodynamics of the SI thermochemical cycle is the electrolyte–NRTL model [6]. The electrolyte–NRTL model has the ability to predict reaction and phase (vapor-liquid and liquid-liquid) equilibria, it includes the effect of temperature and it can handle multiple-electrolyte solutions. As the ability of this model to extrapolate is of high importance for the SI process, its thermodynamic consistency was extensively examined. Although the thermodynamic consistency of any excess Gibbs free energy model is a priori guaranteed, under its specific assumptions, the effect of these assumptions on the derivation of the excess Gibbs free energy that is used to calculate the activity coefficients can be crucial. In the electrolyte–NRTL model the existence of different ions of the same charge sign is modeled with the use of mixing rules for the reference states and the interaction parameters. The effect of these mixing rules is not always evident, because ultimately the model is fitted against experimental data. But, when the accurate prediction of detailed speciation is important, these mixing rules become of higher significance.

An alternative formulation for the electrolyte-NRTL model was developed. The changes can be summarized as the substitution of the Pitzer-Debye-Hückel [35] equation with a detailed form of the original Debye-Hückel model [19] and the inclusion of hydration chemistry in the model in a way that reflects the effect of hydration on the structure of the solution. Hydration is considered for both the cations and the anions and the hydration numbers are allowed to receive negative values representing the effect of the ions on the structure of the solvent. The distance of closest approach of the ions that is inherent as an adjustable parameter in the Debye-Hückel theory is expressed as a function of the radii of the ions and their hydration layer. Two different assumptions were considered for the hydration numbers of the ions: i) that they are independent of the concentration and the activity of the solvent and ii) that they are function of the short-range activity of the solvent (water). The second model was applied to electrolytes consisting of ions that are known to bind with water molecules and show extensive hydration. The models were applied to an extensive database of uni-univalent and bi- and tri-valent electrolytes with considerable success. The model equations are summarized in the following paragraphs.

The short-range interactions are modeled on the basis of the non-random two-liquids (NRTL) model. To account for the short-range interactions three types of local neighborhoods are considered: the immediate neighborhoods of cations, anions and molecular species. The "effective" mole fractions of the local neighborhoods of the original electrolyte-NRTL formalism are replaced by the effective mole fractions of the hydrated solution. For a single strong electrolyte these mole fractions are defined as:

$$X_w = \frac{n_w^o - \sum_i n_i h_i}{n_w^o - \sum_i n_i h_i + \sum_i n_i},\ X_i = \frac{n_i}{n_w^o - \sum_i n_i h_i + \sum_i n_i},$$

where i stands for the ionic species only. The short-range activity coefficients of the hydrated cations and anions in the symmetrical scale are given as:

$$\begin{aligned}
\ln \gamma_c^{SR} &= \sum_a \frac{X_a}{\sum_{a'} X_{a'}} \frac{\sum_j X_j G_{jc.ac} \tau_{jc.ac}}{\sum_j X_j G_{jc.ac}} \\
&+ \sum_m \frac{X_m}{\sum_j X_j G_{jm}} \left[\begin{array}{l} G_{cm} \left(\tau_{cm} - \frac{\sum_j X_j G_{jm} \tau_{jm}}{\sum_j X_j G_{jm}} \right) + \\ \sum_a \frac{X_a}{\sum_{c'} X_{c'}} \left(G_{ca.m} - G_{am} \right) \left(\frac{\alpha_{ca.m} \tau_{am} - 1}{\alpha_{ca.m}} - \frac{\sum_j X_j G_{jm} \tau_{jm}}{\sum_j X_j G_{jm}} \right) \end{array} \right] \\
&+ \sum_a X_a \left\{ \begin{array}{l} \sum_{c'} \frac{X_{c'}}{\sum_{c''} X_{c''}} \frac{1}{\sum_j X_j G_{ja.c'a}} \left[G_{ca.c'a} \left(\tau_{ca.c'a} - \frac{\sum_j X_j G_{ja.c'a} \tau_{ja.c'a}}{\sum_j X_j G_{ja.c'a}} \right) + \right. \\ \left. \sum_m \frac{X_m}{\sum_{c''} X_{c''}} G_{ma.c'a} \frac{G_{ca.m} - G_{am}}{G_{am}} \left(\frac{\alpha_{ca.m} \tau_{ma.c'a} - 1}{\alpha_{ca.m}} - \frac{\sum_j X_j G_{ja.c'a} \tau_{ja.c'a}}{\sum_j X_j G_{ja.c'a}} \right) \right] + \\ \frac{1}{\sum_{c''} X_{c''}} \left(\frac{\sum_j X_j G_{ja.ca} \tau_{ja.ca}}{\sum_j X_j G_{ja.ca}} - \sum_{c'} \frac{X_{c'}}{\sum_{c''} X_{c''}} \frac{\sum_j X_j G_{ja.c'a} \tau_{ja.c'a}}{\sum_j X_j G_{ja.c'a}} \right) \end{array} \right\},
\end{aligned} \tag{22}$$

$$
\begin{aligned}
\ln\gamma_a^{SR} &= \sum_c \frac{X_c}{\sum_{c'} X_{c'}} \frac{\sum_j X_j G_{ja.ca}\tau_{ja.ca}}{\sum_j X_j G_{ja.ca}} \\
&+ \sum_m \frac{X_m}{\sum_j X_j G_{jm}} \left[\begin{array}{l} G_{am}\left(\tau_{am} - \frac{\sum_j X_j G_{jm}\tau_{jm}}{\sum_j X_j G_{km}}\right) + \\ \sum_c \frac{X_c}{\sum_{a'} X_{a'}} \left(G_{ca.m} - G_{cm}\right)\left(\frac{\alpha_{ca.m}\tau_{cm}-1}{\alpha_{ca.m}} - \frac{\sum_j X_j G_{jm}\tau_{jm}}{\sum_j X_j G_{jm}}\right) \end{array} \right] \\
&+ \sum_c X_c \left\{ \begin{array}{l} \sum_{a'} \frac{X_{a'}}{\sum_{a''} X_{a''}} \frac{1}{\sum_j X_j G_{jc.a'c}} \left[G_{ac.a'c}\left(\tau_{ac.a'c} - \frac{\sum_j X_j G_{jc.a'c}\tau_{jc.a'c}}{\sum_j X_j G_{jc.a'c}}\right) + \right. \\ \left. \sum_m \frac{X_m}{\sum_{a''} X_{a''}} G_{mc.a'c} \frac{G_{ca.m}-G_{cm}}{G_{cm}} \left(\frac{\alpha_{ca.m}\tau_{mc.a'c}-1}{\alpha_{ca.m}} - \frac{\sum_j X_j G_{jc.a'c}\tau_{jc.a'c}}{\sum_j X_j G_{jc.a'c}}\right)\right] + \\ \frac{1}{\sum_{a''} X_{a''}} \left(\frac{\sum_j X_j G_{jc.ac}\tau_{jc.ac}}{\sum_j X_j G_{jc.ac}} - \sum_{a'} \frac{X_{a'}}{\sum_{a''} X_{a''}} \frac{\sum_j X_j G_{jc.a'c}\tau_{jc.a'c}}{\sum_j X_j G_{jc.a'c}}\right) \end{array} \right\} .
\end{aligned}
\tag{23}
$$

The short-range activity coefficient of the uncharged species is:

$$
\begin{aligned}
\ln\gamma_m^{SR} &= \frac{\sum_j X_j G_{jm}\tau_{jm}}{\sum_j X_j G_{jm}} + \sum_{m'} \frac{X_{m'} G_{mm'}}{\sum_j X_j G_{jm'}} \left(\tau_{mm'} - \frac{\sum_j X_j G_{jm'}\tau_{jm'}}{\sum_j X_j G_{jm'}}\right) \\
&+ \sum_c \sum_a \frac{X_a}{\sum_{a'} X_{a'}} \frac{X_c G_{mc.ac}}{\sum_j X_j G_{jc.ac}} \left(\tau_{mc.ac} - \frac{\sum_j X_j G_{jc.ac}\tau_{jc.ac}}{\sum_j X_j G_{jc.ac}}\right) \\
&+ \sum_a \sum_c \frac{X_c}{\sum_{c'} X_{c'}} \frac{X_a G_{ma.ca}}{\sum_j X_j G_{ja.ca}} \left(\tau_{ma.ca} - \frac{\sum_j X_j G_{ja.ca}\tau_{ja.ca}}{\sum_j X_j G_{ja.ca}}\right) .
\end{aligned}
\tag{24}
$$

The above equations are given for the general case of mixed-solvent, multi-electrolyte solutions. In the above equations all the non-randomness factors ($\alpha_{ca.m}$, $\alpha_{m.ca}$, $\alpha_{ca.ca'}$) are considered equal (typically, being assigned the value of 0.2 for salt-solvent, salt-salt interactions). The assignment of a constant value to the non-randomness factors of all the electrolytes was found satisfactory in this work and was used to minimize the number of adjustable parameters. The analytical expressions for the case of different non-randomness factors for each electrolyte have been given elsewhere [2].

The long-range activity coefficients are calculated on the unsymmetrical scale by

$$
\ln\gamma_i^{*,\,DH} = -\frac{\mathcal{F}^2}{4\pi\varepsilon_o\varepsilon_s\mathcal{R}T}\frac{\kappa z_i^2}{6\mathcal{N}_A}\left(2\chi\left(\kappa a_i\right) + \frac{\sum_k n_k z_k^2\sigma_k}{\sum_k n_k z_k^2}\right) + \frac{\bar{V}_j}{\mathcal{R}T}\frac{\mathcal{F}^2}{4\pi\varepsilon_o\varepsilon_s}\frac{\kappa}{6\mathcal{N}_A V}\sum_k n_k z_k^2\sigma\left(\kappa a_k\right) , \tag{25}
$$

for ions and

$$
\ln\gamma_m^{*,\,DH} = \frac{\bar{V}_m}{\mathcal{R}T}\frac{\mathcal{F}^2}{4\pi\varepsilon_o\varepsilon_s}\frac{\kappa}{6\mathcal{N}_A V}\sum_i n_i z_i^2\sigma\left(\kappa a_i\right) , \tag{26}
$$

where a is the distance of closest approach and $\bar{V}_j$ the partial molar volumes of the ions and the molecular species. The radii and the infinite dilution partial molar volumes of the ions are taken from Marcus [27]. The radius of water in the hydration shell, $r_{w,ca}^{els}$, for 1-1 electrolytes is taken from Marcus [27] equal to 0.18687 nm. For 1-2, 2-1, 3-1 and 2-2 electrolytes $r_{w,ca}^{els}$ was fitted to experimental data and found to be 0.15703, 0.17719, 0.14253, 0.02400 nm, respectively.

Eqs. (22) - (24) give the rational activity coefficients of the hydrated solution on the symmetrical scale, while Eqs. (25) and (26) give the unsymmetrical rational activity coefficients of the solution, considered unhydrated. The short-range activity coefficients can be converted to the unsymmetrical form by the traditional relationship:

$$
\ln\gamma^{*,\,SR} = \ln\gamma^{SR} - \ln\gamma^{SR,\infty}
$$

and for the calculation of the total deviation from ideality the additivity assumption for the activity coefficients is utilized:

$$
\ln\gamma^{*} = \ln\gamma^{*,\,SR} + \ln\gamma^{*,\,DH}.
$$

The mean molal stoichiometric activity coefficients of the solution considered unhydrated, that can be compared with the experimentally measured values, are calculated as:

$$
\ln\gamma_{\pm}^{*,\,\mathrm{m}} = \ln\gamma_{\pm}^{*,\,(h)} - \frac{h_{ca}}{v_{ca}}\ln a_w^{*,\,SR} - \ln\left(1 + n_{ca}^o\frac{v_{ca}-h_{ca}}{n_w^o}\right) , \tag{27}
$$

for the constant hydration model and

$$\ln \gamma_{\pm}^{*,\,\mathrm{m}} = \ln \gamma_{\pm}^{*,\,(h)} + \ln\left(\frac{n_w^o}{\sum_j n_j}\right) + \frac{v_c q_{hca}}{v_{ca}} \ln \frac{1 + k_{hca}}{1 + k_{hca}\, a_w^{SR}} \ , \tag{28}$$

for the model utilizing stepwise hydration equilibria to model highly hydrated electrolytes up to their solubility limit, with $q_{hca}(= 4)$ and k_{hca} assigned to the cation and considered as electrolyte-specific properties.

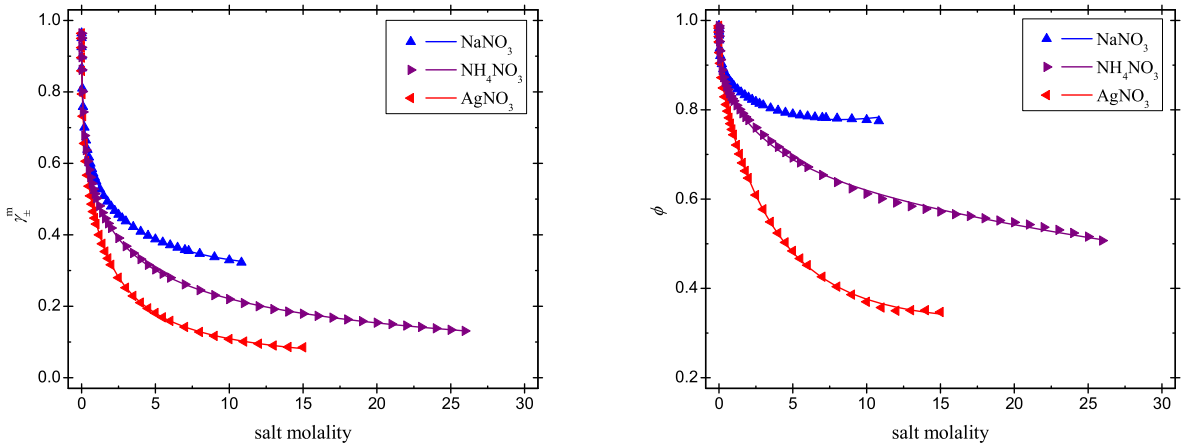

Figure 36: Application of the constant hydration model for nitrate electrolytes up to very high concentrations, (a) prediction of molal mean ionic activity coefficients, (b) prediction of osmotic coefficients

Figures 36 (a) and (b) show the excellent fit of the model for weakly or negatively hydrated electrolytes up to their solubility limit, while the results of applying Eq. (28) to the experimental data of activity and osmotic coefficients of lithium- chloride, bromide and nitrate are shown in Figure 37. The application of the model to the majority of aqueous single-electrolyte solutions was performed to examine the accuracy and consistency of the model. Accuracy and thermodynamic consistency guarantee that the model can be extrapolated to higher temperatures with a minimum error expectancy, something crucial for modeling the thermodynamics of the Sulfur-Iodine thermochemical cycle. Details on the derivations, formulations and applications of the refined electrolyte-NRTL model can be found in a paper submitted to *Fluid Phase Equilibria*.

The refined activity coefficient formulations shown in the Eqs. (22), (23) and (24) are considerably more complex than those of the original electrolyte-NRTL model. Their advantage is thermodynamic consistency. To illustrate the inconsistency referred to, it was verified that minimization of the Gibbs free energy does not yield the same result as the so-called equilibrium constant method using the activity coefficients of the original electrolyte-NRTL model, in the case of partially dissociated multi-electrolyte systems. Moreover, the refined formulation provides stronger predictive capability for multi-electrolyte solutions. A simple example of the latter is given in Figure 38, where the effect of mixing sodium chloride with potassium chloride in aqueous solutions of constant total molality is shown. The mean activity coefficient of each salt as predicted by the two models (the original electrolyte-NRTL - Figure 38(a) and the new formulation denoted as "refined eNRTL" - Figure 38(b)) for various salt-salt interaction parameters are compared with the experimentally measured values. In this case study the values of the binary interaction parameters of the original eNRTL model were used for both models (for single-electrolyte aqueous solutions both models are identical). Comparison of the Figures 38(a) and (b) shows that the new activity coefficient formulation

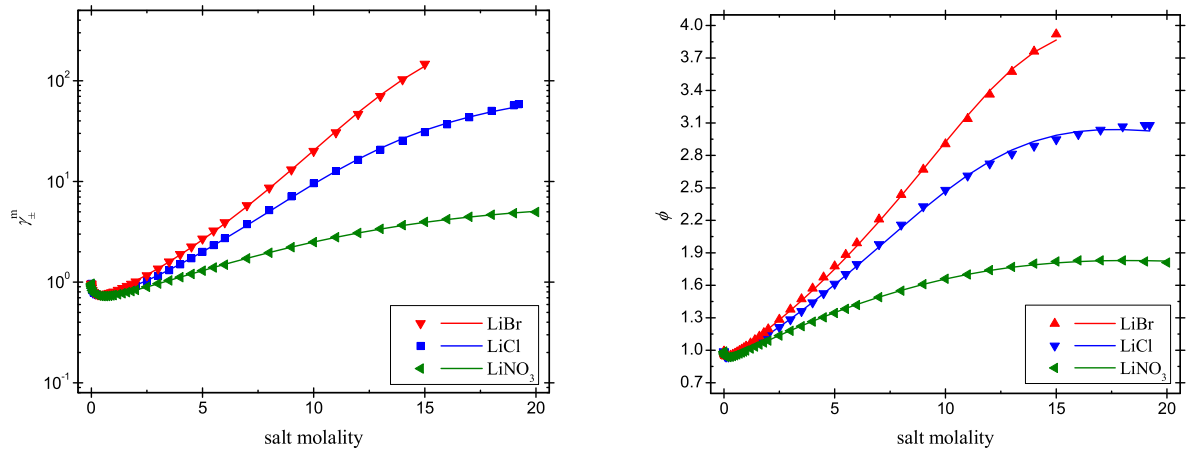

Figure 37: Application of the stepwise hydration equilibria model for lithium electrolytes up to very high concentrations, (a) prediction of molal mean ionic activity coefficients, (b) prediction of osmotic coefficients

provides more reliable extrapolation capability for the mixing of the electrolytes, while both models broadly follow the basic principle of the Harned's rule, i.e., the mean ionic activity coefficient of one electrolyte in an aqueous mixture of electrolytes of constant total molality is directly proportional to the molality of the other electrolyte. ASPEN Technology plans on implementing the refined model in the aspenONE software.

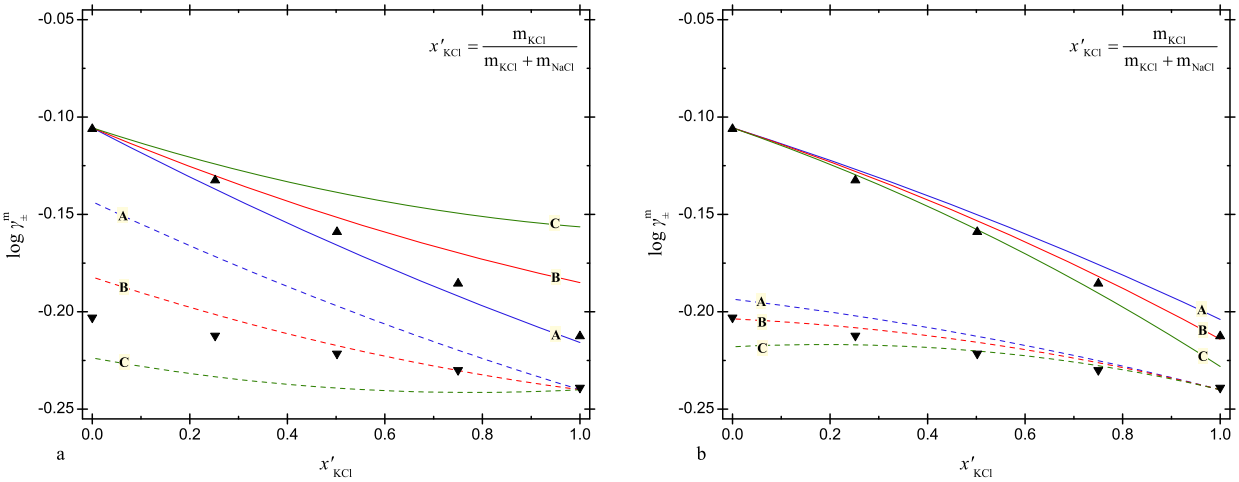

Figure 38: Harned's rule plot of mean ionic activity coefficient of the NaCl-KCl-H2O solution at constant total molality of 4 (a) original eNRTL and (b) refined eNRTL (solid lines represent the mean activity coefficient of NaCl, dashed lines represent the mean activity coefficient of KCl; A: $\tau_{NaCl.KCl} = 0.00$; B: $\tau_{NaCl.KCl} = 0.25$; C: $\tau_{NaCl.KCl} = 0.50$; the data points are the respective experimental values).

The consistent derivation of the excess Gibbs free energy of the electrolyte-NRTL formalism as applied to the aqueous solution of sulfuric acid at ambient conditions is presented in Figures 39–41. The aqueous sulfuric acid system, even at ambient conditions, poses great challenges for the existing electrolyte models. Reasons

include the partial dissociation of the bisulfate ion, the hydronium and bisulfate complex formation, the different extents of proton hydration (with respect to the initial H_2SO_4 molality) and the partial dissociation of the sulfuric acid at high concentrations (because of the elimination of free water). Furthermore, the sulfuric acid water mixture (although a binary system) is in fact a multi-electrolyte (because of the coexistence of the bisulfate and sulfate anions) and mixed-solvent (because of the formation of complexes and the partial dissociation of the sulfuric acid at high concentrations) system. To show the significance of appropriately including the mixing rules in the short-range interaction excess Gibbs free energy term and the corresponding activity coefficients, both the original electrolyte-NRTL and the new formulation were fitted against available experimental data for the aqueous sulfuric acid system at ambient conditions. For this demonstration the constant hydration model was used and consequently both models were fitted to the experimental database restricted to initial H_2SO_4 concentrations up to 20 molal. The results of the best fit of both models are presented in Figure 39. It is evident that the original electrolyte–NRTL model fails in predicting together the mean molal stoichiometric activity coefficient of the solution and the degree of dissociation of the bisulfate. On the other hand, the new formulation (denoted in all plots as "corrected eNRTL") simulates the system satisfactorily.

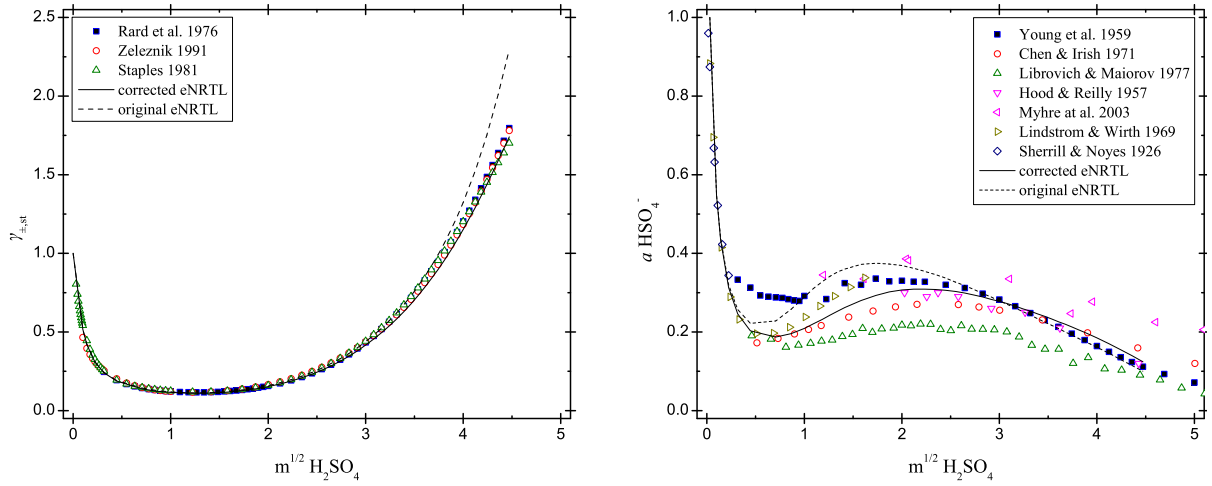

Figure 39: Model predictions and experimental measurements of (a) the mean molal stoichiometric activity coefficient and (b) the degree of dissociation of the bisulfate ion vs. square root of the initial molality of sulfuric acid at concentrations up to 20 molal (using a constant hydration number).

As a second step, the capability of the new formulation to extrapolate to higher concentrations using a function for the hydration number was examined. To examine the capability of the model to extrapolate and to demonstrate the importance of appropriately including the mixing rules before the derivation of the short-range activity coefficients, the model was fitted to experimental data up to 50 m and then used to predict the speciation and water activity of the solution up to 65 m. The results of the fit and extrapolation of the model are presented in Figures 40–41. It is evident that the new formulation of the electrolyte–NRTL model is able to satisfactorily describe and predict the sulfuric acid solution, even at very high concentrations. The prediction of speciation presented in Figure 40 demonstrates that the model is capable of capturing the actual chemistry of the system and, therefore, it can be used for kinetic studies of the system.

The application of the refined electrolyte-NRTL model to the binary solutions of sulfuric acid and hydrogen iodide with water at temperatures of the Bunsen reaction range is very satisfactory, as shown in Figures 42 and 43. A very accurate prediction of the azeotropes of both solutions is presented, while speciation prediction (for the sulfuric acid solution, where speciation data exist) at ambient conditions is as shown

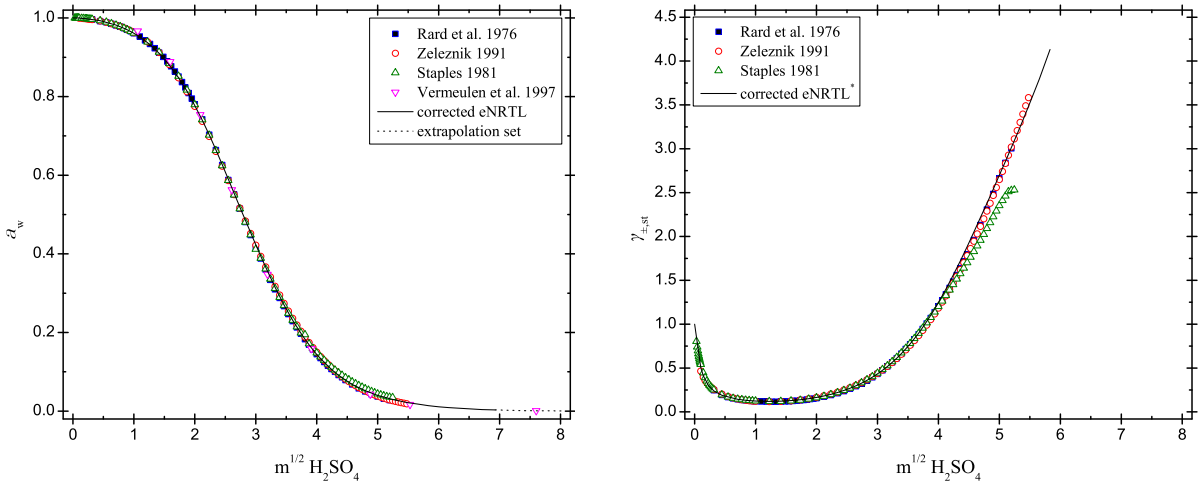

Figure 40: Model predictions and experimental measurements of (a) the activity of water and (b) the mean molal stoichiometric activity coefficient vs. square root of the initial molality of sulfuric acid at concentrations up to 65 molal (data above 50 molal were not included in the fitting database - they show the extrapolation ability of the model).

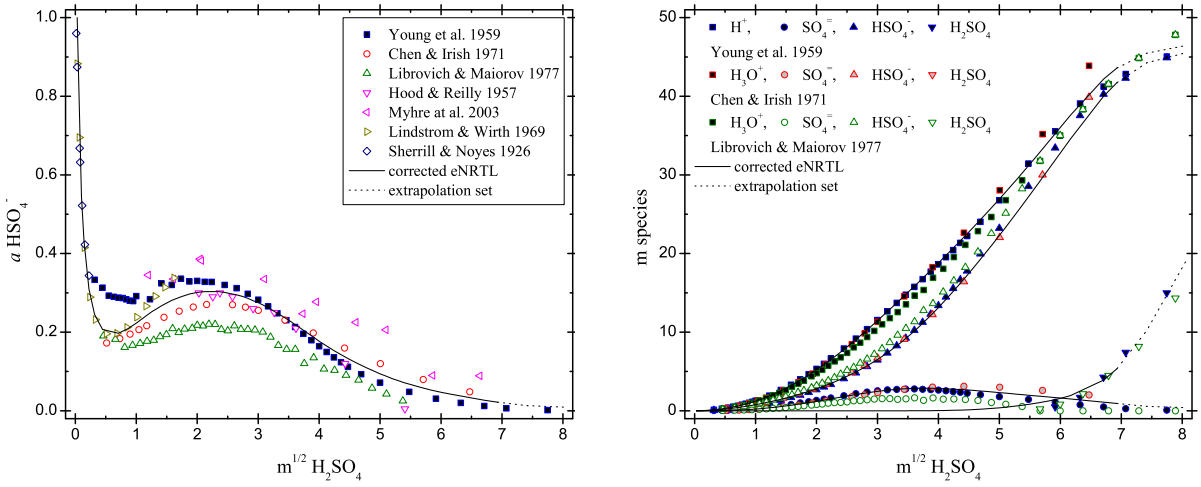

Figure 41: Model predictions and experimental measurements of (a) the degree of dissociation of the bisulfate ion and (b) the detailed speciation vs. square root of the initial molality of sulfuric acid at concentrations up to 65 molal (data above 50 molal were not included in the fitting database - they show the extrapolation ability of the model).

in Figure 41. Thermodynamic data are required to validate the model performance for the ternary solution.

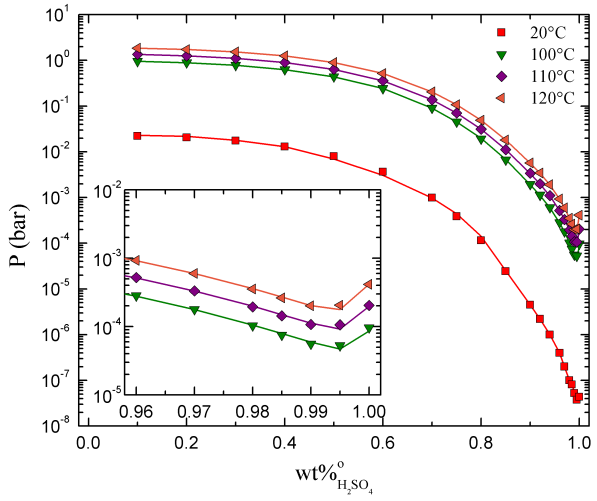

Figure 42: Isothermal phase diagram prediction for the H_2SO_4-H_2O solution.

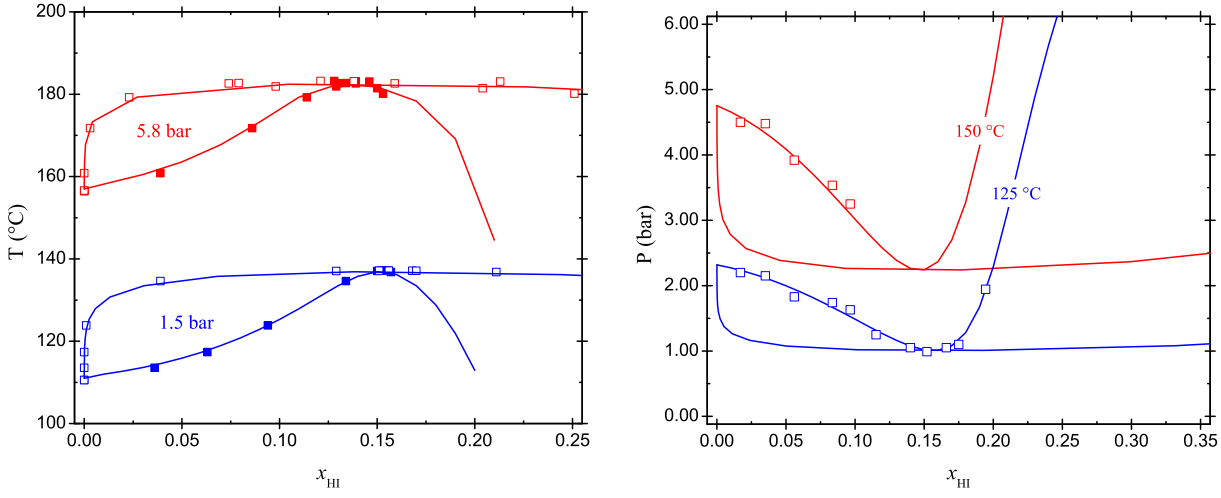

Figure 43: Isobaric and isothermal phase diagram prediction for the HI-H_2O solution.

4.3 Parameter Estimation and Phase Stability in Phase Equilibrium Problems

One of the main problems that are inherent in modeling the thermodynamics of the SI thermochemical cycle is the fitting of the parameters of the model used, such as the electrolyte-NRTL and NRTL models, to the experimental data. The main reason for this is the difficulty in obtaining a good fit for the thermodynamic properties measured that would be valid and consistent with the number of phases of the real solution studied. Reliable computation of phase equilibria can be performed by formulating the problem as a nonlinear program (NLP) for global minimization of the Gibbs free energy of the system, subject to mass balance constraints. For the calculation of the values of the parameters for the thermodynamic models used to describe phase equilibrium an analogous procedure should be followed. The fitting of model parameters to experimental data using the Gibbs free energy minimization approach results in a bilevel optimization problem. Solving the inner optimization problem (i.e., Gibbs free energy minimization) with a global solver guarantees for the stability of the model prediction within the composition range examined. Moreover, requiring that a phase stability criterion constraint is satisfied in the whole of the composition space guarantees global stability of the solution. The new formulation was applied to problems from the literature, in which inappropriate fitting of the parameters of the NRTL model to experimental data has been reported to result in significant model errors. Excess Gibbs free energy models such as the NRTL model [37], are flexible and capable of predicting liquid-liquid equilibria. However, the flexibility of these models is at the same time their weakness. In many cases ([16], [30] and [43]) it has been reported that these models are so flexible that in practice they tend to predict more liquid splits than actually exist in the real system studied. Generally, this is overcome by checking the stability of the model predictions when fitting the model parameters, as discussed by Sørensen and Arlt [42].

One of the main advantages of local composition models, such as the NRTL model, is that they are predictive, in the sense that ternary and quaternary systems can be modeled with knowledge of the interaction parameters of all the possible binaries involved. Hence, the general case of fitting parameters of a local composition model is to fit parameters for binary systems and then use those for predicting the behavior of systems with a larger number of species. The Gibbs phase rule states that a binary liquid system can form a maximum of four phases at given temperature and pressure, but real liquid systems usually show a maximum of two liquid phases at variable temperature and pressure. In other words, thermodynamic models are capable of predicting very complex behaviors, but nature is usually simpler than the model.

Considering only liquid phase systems, the illustrative example in Figure 44 demonstrates the problems that can be caused by using an inappropriate set of parameters in the NRTL model. Consider a hypothetical binary liquid system of components (1) and (2) with a measured liquid split at mole fractions $x_1^{l_1} = 0.1$ and $x_1^{l_2} = 0.9$. For different sets of binary parameters and non-randomness factors (see Figure 44) the NRTL model can predict a maximum of three liquid phases that show a local minimum for the Gibbs free energy of mixing at the specified compositions. Five main categories can be distinguished for the phase behavior the NRTL model predicts, depending on the parameters used, which all satisfy the phases iso-activity condition:

- *Category A:* Curve A in Figure 44 corresponds to a stable liquid split with no metastable states. This was set as an objective in the parameter estimation algorithm in the original work by Sørensen and Arlt [42] and the supplementary work by Macedo and Rasmussen [25]. The method applied by these researchers was to check the sign of $\partial^2 \Delta g / \partial x_1^2$ in the whole concentration range and for all the LLE systems examined and discard all the solutions that contain more inflection points than necessary to describe the phase split. As discussed by Simoni et al. [41], the use of advanced modern methods for phase equilibrium calculations, such as the Gibbs free energy minimization or Gibs tangent plane stability test, constitute this constraint unnecessary.

- *Category B:* Curve B shows a liquid split with a metastable state. The model predicts a stable phase split at the "experimental" compositions, but care must be taken when using such a set of parameters for the model, because a local method (iso-activity or Gibbs free energy minimization with a local solver) may return the unstable intermediate split as the solution.

- *Category C:* Curve C shows a stable three liquid phase system. The model predicts two phases with the "experimental" compositions, but also the existence of a third phase. The prediction is consistent with Gibbs' phase rule but not with what was (hypothetically) measured.
- *Category D:* Curve D corresponds to two liquid splits within the hypothetically measured compositions. That is, a local solution exists at the "measured"compositions, but the global solution corresponds to two stable phase splits.
- *Category E:* Curve E shows two liquid splits with the second one outside the (hypothetically) measured compositions. The "measured"compositions here are $x_1^{l_1} = 0.01$ and $x_1^{l_2} = 0.3$. Obviously, the whole composition space should be studied, because there might be other stable splits outside the composition region examined. This example demonstrates that even when the stability test for the composition region studied is satisfied, the whole composition space should always be checked for potential other phase splits.

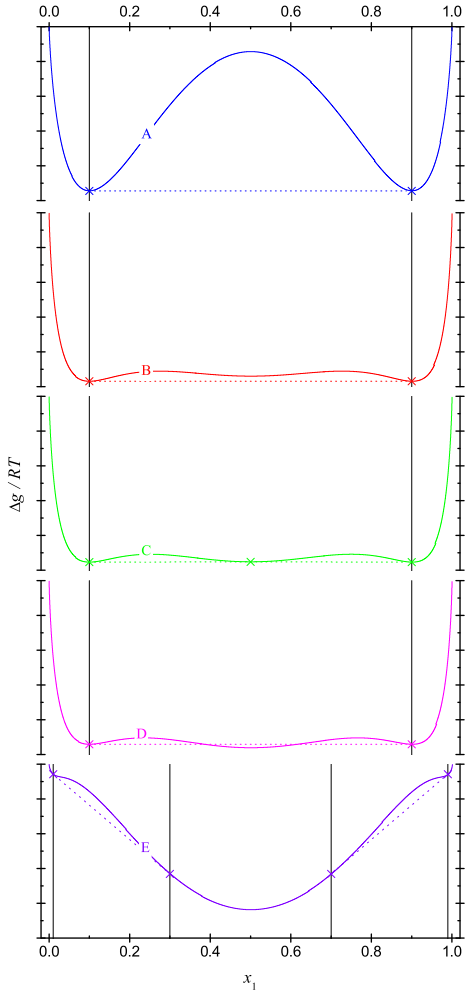

Figure 44: Phase behavior categorization of the properties of the NRTL model. (—A—: $\tau_{ij} = 1.62525$, $\alpha_{ij} = 0.2$; —B—: $\tau_{ij} = 2.57726$, $\alpha_{ij} = 0.42479$; —C—: $\tau_{ij} = 2.60012$, $\alpha_{ij} = 0.42606$; —D—: $\tau_{ij} = 2.61862$, $\alpha_{ij} = 0.42701$; —E—:$\tau_{ij} = 4.11456$, $\alpha_{ij} = 0.46682$)

For the remaining of this report these five cases will be referred to as "phase behavior categories" A, B,

C, D and E, respectively. It should be noted that equivalent real examples for all of the hypothetical cases presented in Figure 44 can be found in the literature. Real literature examples have been examined and the new formulation has been applied with considerable success. The point illustrated in Figure 44 is that, unless some kind of stability test is applied during the fitting of the model parameters, it is possible to get an excellent fit that belongs to any one of these five phase behavior categories. Of course, for the binary system postulated, it is known from the experiment that only two phases are present in the liquid solution, hence the possibility for the model to predict any of the behaviors C, D and E should be excluded form the solution. For instance, using the iso-activity method discussed in Ref. [42] can result in an excellent fit that could belong to any of the described five phase behavior categories.

Sørensen and Arlt [42] and Macedo and Rasmussen [25] plot the Gibbs tangent plane diagram of each examined system and discard all the solutions that have more inflection points than necessary for the description of the liquid split. However, it is unclear what one should do if during the fitting of the parameters of the model a solution is found that belongs to phase behavior categories B, C, D or E. Moreover, there might be systems for which the best fit is achieved if more inflection points are allowed to exist (as in curve B of Figure 44), yet only one stable phase split is predicted by the model. Simoni et al. [41] present an interval Newton algorithm that can be used to find all the possible solutions for the binary parameters that satisfy a measured liquid split at a specified temperature. It is, however, admissible that the phase split at a specific temperature is not of much use for real engineering problems, where temperature is a design and operating variable of the process and can and will change during process operation. The inclusion of the dependence of the model parameters on temperature results in an optimization problem, in which there exist not a solution but "best fit values" for the model parameters. The proposed formulation for consistently and accurately fitting the model parameters to the experimental data addresses this optimization problem.

The fitting of the model parameters (P_i) to the experimental data using the problem formulation of Eq. (29) gives rise to a bilevel optimization problem. That is, the models are fitted to the experimental data, whereas solving at each experimental data point the problem of Eq. (29). An optimization framework for this task has been developed, which covers the cases of fitting the parameters of the NRTL model to liquid-liquid, vapor-liquid and vapor-liquid-liquid equilibrium problems.

$$\begin{aligned} &\min_{P_i} \left[\text{discrepancy between predicted and observed system properties}\right] \\ &s.t. \min_{N_j} G \\ &s.t. \text{ problem equations} \end{aligned} \tag{29}$$

The detailed formulation of Eq. (29) involves very complex mathematics and is beyond of the scope of this report; the complete formulation can be found in Refs. [32, 1]. The parameter estimation was cast as a bilevel program with multiple lower-level programs, corresponding to (generalized) semi-infinite constraints given by the requirements for (*i*) stability of the predicted phase-split, (*ii*) excluding additional spurious phase splits and (*iii*) predicting the correct number of phases in each phase split. Global optimization techniques are necessary for the lower-level program since otherwise the model predictions may correspond to unstable phase splits. Additionally, global solution of the upper-level program gives a certificate of optimality which is useful in the case of model-experiment mismatch. The formulation developed is independent from the thermodynamic model used for predicting phase equilibria, and does not require any specific structure of the system. The detailed formulation of the program involves a significant amount of mathematics and it is beyond the scope of this report. Details and examples of its application to LLE problems can be found in Ref. [32]. The model has been extended for application to solutions exhibiting VLE and VLLE and azeotropic behavior [1]. Two typical examples of the application of the bilevel optimization formulation are given in the following for parameter estimations in binary solutions exhibiting LLE and VLLE.

The liquid-liquid equilibrium of the system n-butyl-acetate-water was originally studied by Heidemann and Mandhane [15] in an effort to examine the properties of the NRTL model. Heidemann and Mandhane presented parameter values for which the NRTL model predicts two phase splits, whereas data exhibiting

one phase split were used for the fitting of the binary parameters. The conclusion of their work was that the NRTL model is capable of predicting very complex behaviors, however one should cautiously examine the predicted phase behavior of the model for extra inflection points that may predict other or more stable phase splits than those that actually exist in the real system. Later, Mandhane and Heidemann [26] presented alternative values for the binary parameters for the n-butyl-acetate-water system, with the use of which the model does not exhibit such complex behavior and correlated the data equivalently well. The Gibbs free energy tangent plane plots for three parameter values are presented in Figure 45. The first two (S1 and S2) are due to Refs. [15, 26] and the third (S3) due to Ref. [25]. The parameter values S1 are obviously wrong, as they predict two phase splits. The parameter values S2 are correct but a global solver has to be used for the prediction of the stable phase split. Finally, those of S3 predict a Gibbs surface without additional inflection points. The comparison of measurements and predictions, using the parameters calculated with the bilevel formulation, is given in the T-x plot of Figure 46. Both absolute and relative error are very small.

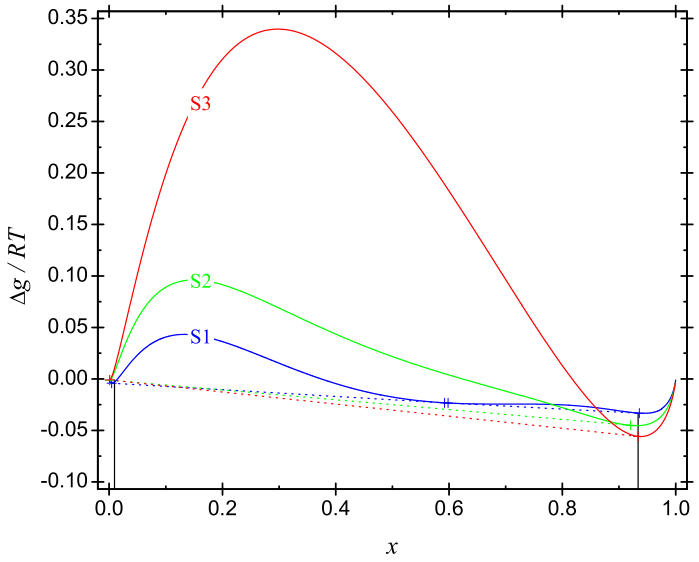

Figure 45: Gibbs free energy tangent plane diagram for the system n-butyl-acetate (1) – water (2) using literature values for the NRTL binary parameters. (—S1— : Ref. [15] $\alpha_{ij} = 0.3917$, $\tau_{12} = 3.00498$, $\tau_{21} = 4.69071$; —S2—: Ref. [26] $\alpha_{ij} = 0.35$, $\tau_{12} = 2.62870$, $\tau_{21} = 5.71860$; —S3—: Ref. [25]) $\alpha_{ij} = 0.2$, $\tau_{12} = 0.16643$, $\tau_{21} = 6.02012$. The vertical lines show the smoothed experimental data from Ref. [25].

The qualitative goal in the VL(L)E formulation is the same as in the LLE case. However, the mathematical formulation of the problem is significantly different. The main idea in extending the formulation to the asymmetric case is to utilize a hypothetical single phase with the Gibbs free energy $G = \min\{G^L, G^V\}$. Note that the min −function causes the Gibbs free energy function to be nondifferentiable. In VLE and VLLE the measurements typically include the temperature and pressure of the system and the compositions of each phase. In the bilevel framework proposed, it is the modeler's choice which of these intrinsic properties will be considered as fixed and which as variable. In the following, the optimization variables are the temperature coefficients of the excess Gibbs free energy model and the mole fractions in each phase. The pressure and temperature can be fixed parameters $T^{pred,i} = T^{meas,i}$ and $P^{pred,i} = P^{meas,i}$ or they can be included in the optimization program as variables fitted against their measured variables. In the simple case where temperature and pressure are considered as fixed parameters, the goal of the optimization problem is to find the temperature coefficients of the excess Gibbs free energy model, such that the model predicts a minimal

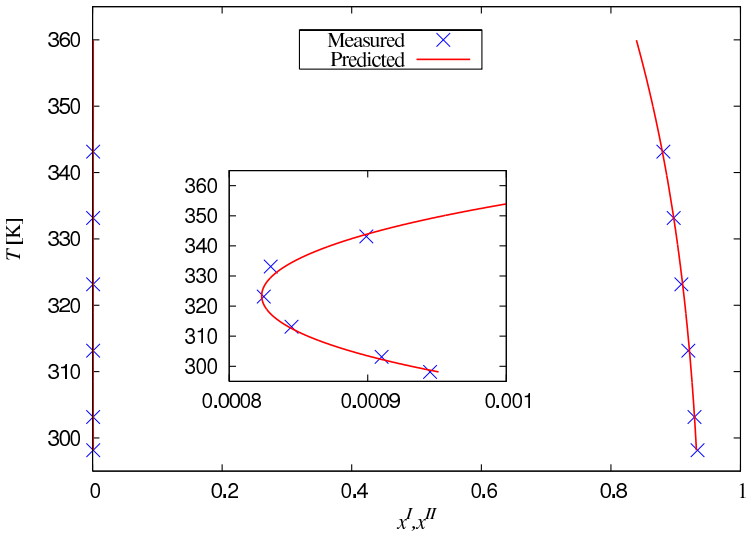

Figure 46: T-x plot for the system n-butyl-acetate (1) – water (2) using the estimated parameters for the temperature dependence.

deviation of the mole fractions from their measured valued at the measured temperature and pressure:

$$f^* = \sum_{i=1}^{n_e} \sum_{k=I}^{n_p^i} w^{i,k} (x^{meas,i,k} - x^{pred,i,k})^2,$$

where the absolute objective function is used, with scaling allowed via the weights $w^{i,k}$. An interesting point is how azeotropes are encoded within the proposed framework. Azeotropes can, but need not be treated in a special way. In binary systems heterogeneous azeotropes have three phases and can be directly implemented in the formulation. On the other hand, homogeneous azeotropes have the special property that the two phases are identical. This can be easily imposed as an additional equality constraint, or by elimination of one of the variables. It should be noted that it is not always necessary or advisable to do so. For instance, when many measurements are available around the azeotropic point, there is no need to specifically define the azeotropic point. An example of the application of the bilevel parameter estimation framework to a system exhibiting VLE is given in the following.

Experimental data for the vapor-liquid equilibrium of the system 2-methyl-2-butene (1) - methanol (2) at system pressure of 101.3 kPa and within the temperature range of 305 to 340 K are included in the VLE Data Collection published by DECHEMA. More recently the system was studied by [38], the measurements of whom are in good agreement with the data included in the DECHEMA data collection. The experimental VLE data of [38] are given in the supplementary material, along with the Antoine constants for the pure components. Parameter values for the Margules, Van Laar, Wilson, NRTL and UNIQUAC models are reported in the DECHEMA VLE data collection for this system. In the modeling of phase equilibrium by [11] the vapor phase is modeled as ideal and the NRTL energy parameters ($\Delta g_{ij} = \tau_{ij} RT$) are considered independent of temperature. According to the DECHEMA VLE data collection the NRTL model is the most accurate in the description of the system 2-methyl-2-butene (1) - methanol (2).

The calculated phase behavior using the NRTL binary parameters given by DECHEMA is presented in Figure 47. A phase split is predicted for the liquid phase, in contrast to the measurements and the measured homogeneous azeotrope is modeled as a heterogeneous one. Analysis of the Gibbs tangent plane diagram for this system (not presented here) shows that the extra inflection point that produces the phase split is almost not evident. This again rises the point that a phase stability test should be implemented in the parameter

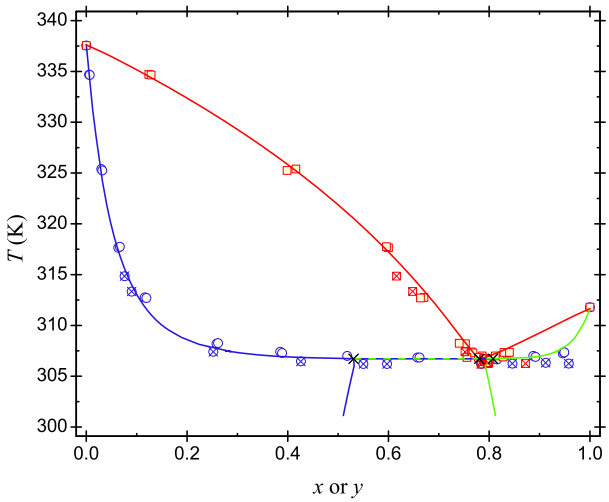

Figure 47: Phase diagram prediction of the system 2-methyl-2-butene (1) – methanol (2); NRTL binary parameters are due to DECHEMA VLE data collection [11]; the measured homogeneous azeotrope is modeled as heterogeneous.

estimation formulation, in order to calculate valid parameter values. Using the experimental VLE data of [38] and the bilevel formulation the calculated phase T-x-y diagram and the optimal model parameters are shown in Figure 48. The fit obtained is very good and no liquid split is predicted with the parameters estimated using the bilevel optimization formulation. The formulation was used for the estimation of parameters a large number of systems that exhibit homogeneous and heterogeneous azeotropes, liquid-liquid equilibrium and vapor-liquid equilibrium at different temperature ranges and biazeotropic behavior.

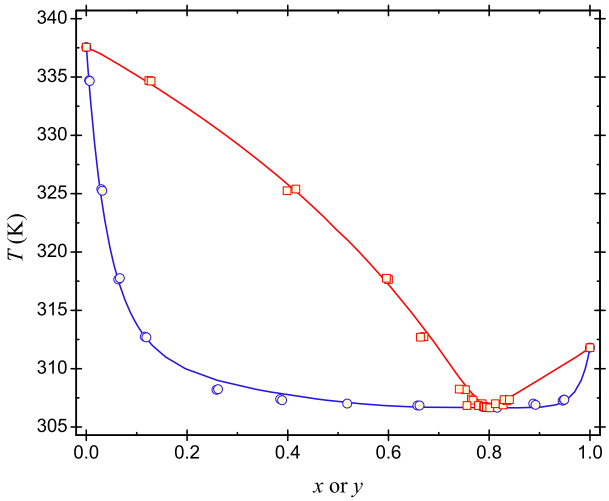

Figure 48: Isobaric phase diagram prediction of the system 2-methyl-2-butene(1) – methanol (2) using the estimated parameters for the NRTL model.

For validation, the formulation was tested against a very difficult phase equilibrium problem, namely the VLLE of the mixture tetrahydrofuran with water. The mixture tetrahydrofuran (1) – water (2) poses much difficulty for thermodynamic models. It shows a closed miscibility gap with a lower critical solution temperature (LCST) at 344.95 K and $x = 0.2198$ and an upper critical solution temperature (UCST) at

410.25 K and $x = 0.1874$. At $P = 101.325$ kPa it exhibits homogeneous azeotropic VLE, with the LCST of its LLE inside the left "banana" of the VLE. At atmospheric pressure, the liquid miscibility disappears because of the formation of vapor phase. Using the bilevel formulation for parameter estimation the entire VLE/LLE phase diagram of this mixture is predicted very accurately, as shown in Figure 49. The point illustrated in Figure 49 is that the use of different types of phase equilibrium data within the proposed formulation for parameter estimation can result in very accurate predictions of the entire phase diagram of a mixture, and this is highly desirable for engineering purposes. It is the first time that such an accurate NRTL model is developed for this challenging mixture.

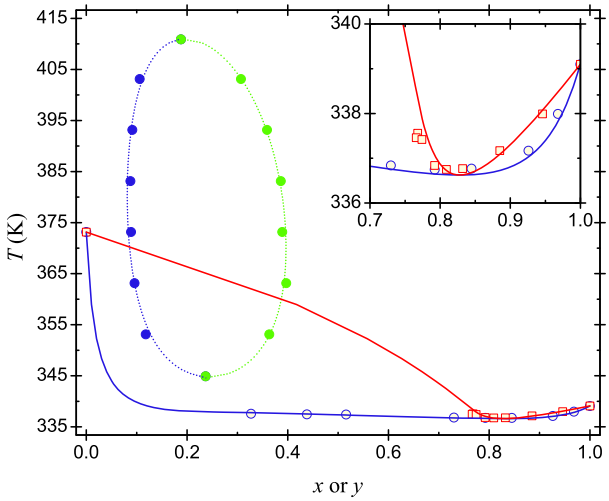

Figure 49: Isobaric VLE phase diagram prediction (at $P = 101.325$ kPa - solid lines) and LLE phase diagram prediction (at higher P - doted lines) of the mixture tetrahydrofuran (1) – water (2), using the NRTL model and the parameter values calculated using the novel bilevel formulation.

The bilevel optimization framework for parameter estimation in phase equilibrium problems would be a very useful tool in estimating parameters for the thermodynamic models applied to the SI process. Future work involves the integration of other types of thermodynamic data (e.g., excess heat of mixing, heat capacities of mixing, etc.) in the bilevel optimization framework and extending the method for application to multi-component solutions. Nonetheless, it should be noted that multiple solutions exist in parameter estimation algorithms for phase equilibrium, among which some might be invalid (unstable) and it is important to take that into account that robust optimization algorithms would increase the accuracy of the models applied and the accuracy of the simulations of the process.

4.4 Thermodynamic data reduction and model application for sulfuric acid and hydrogen iodide

Overall, the majority of the problems related with the uncertainty in modeling of thermochemical cycles lie in the prediction of the thermodynamic properties in the various sections of the process. It has been suggested that mechanisms should be established to stimulate, collect and validate more physical property experimental and modeling work. This would give the opportunity to researchers doing modeling work to validate their models. One of the major difficulties in modeling the SI cycle is the absence of parameters for the electrolyte thermodynamic models at the conditions of interest. Recently, experimental data have become available for some of the process sections, whereas much more are expected in the near future. Hence, a comprehensive framework that deals with all aspects of the thermodynamics of the SI cycle needs to be developed. This framework starts with the development of a self consistent database of thermodynamic

properties for the various sections of the SI thermochemical cycle. For this objective, published azeotropic composition data for the solutions of interest together with high temperature P-T-x data and heat of mixing and mixture heat capacity data were gathered in a database and evaluated critically for self-consistency.

In this work, the treatment of available data for the development of a comprehensive database follows the works of Zeleznik [48] and Bolsaitis and Elliott [3]. A flexible functional form is chosen for the description of the deviation from ideality of the liquid phase, while the gas phase is treated as ideal. The assumption of an ideal gas phase should be valid up to relatively low pressures, and an equation of state could be used for the extrapolation of the model to higher pressures. The model equations are as follows.

$$\frac{G^{(r)}}{RT} = [G(T,P;\mathbf{x}) - G^{\circ}(T,P;\mathbf{x})]/RT = -\sum_{i=1}^{2} A_i \sum_{j=1}^{2}\sum_{k=1}^{2}(B_{ijk} + C_{ijk}\ln x_i)x_j x_k,$$

where

$$\begin{aligned} A_1 &= 1, \\ A_2 &= x_1 x_2, \\ B_{ijk} &= b^1_{ijk}/T + b^2_{ijk}\ln T + b^3_{ijk} + b^4_{ijk}T + b^5_{ijk}T^2, \\ C_{ijk} &= c^1_{ijk}/T + c^2_{ijk}\ln T + c^3_{ijk} + c^4_{ijk}T + c^5_{ijk}T^2. \end{aligned}$$

Using this equation for the relative Gibbs free energy of the liquid phase the enthalpy of mixing is calculated on the basis of the fundamental equation

$$H^{(r)}(T,P;\mathbf{x})/RT = [H(T,P;\mathbf{x}) - H^{\circ}(T^{\circ},P;\mathbf{x})]/RT = \frac{-\partial[G^{(r)}(T,P;\mathbf{x})/RT]}{\partial \ln T},$$

$$C_P(T,P;\mathbf{x}) = C_P^{(r)}(T,P;\mathbf{x}) = \frac{\partial H^{(r)}(T,P;\mathbf{x})}{\partial T},$$

$$RT\ln(\gamma_i) = \mu_i^{(r)} = \mu_i(T,P;\mathbf{x}) - \mu_i^{\circ}(T,P) = \left[1 - \sum_k x_k \frac{\partial}{\partial x_k} + x_i \frac{\partial}{\partial x_i}\right] G^{(r)},$$

where the superscript (r) denotes property relative to the pure species at the reference state at T = 298.15K, P = 0.1MPa.

The model proposed by Zeleznik is somewhat simple because it disregards the dissociation of sulfuric acid in the gas phase and the fact that the vapor in equilibrium with pure sulfuric acid includes $H_2O^{(V)}$, $H_2SO_4^{(V)}$ and $SO_3^{(V)}$. Bolsaitis and Elliott integrated the dissociation reaction to generate a database for activity coefficient and vapor pressure for the three gaseous species, H_2O, H_2SO_4, SO_3:

$$H_2SO_4(g) \rightleftharpoons H_2O(g) + SO_3(g)$$

Bolsaitis and Elliott used $x_{H_2SO_4} = 0.9402$ at $T = 298.15$ K for the azeotropic composition, obtained from studying published azeotropic data for the H_2SO_4-H_2O system. On the basis of this value for the azeotropic composition all other P-T-x data were corrected using the following empirical relationship:

$$x = \frac{x^*(P)}{x^{*'}(P)}x',$$

where $x^*(P)$ and $x^{*'}(P)$ are the trusted and erroneous measured azeotropic compositions, respectively, at P.

In the present work, the model equations and the data used by Bolsaitis and Elliott [3], Zeleznik [48], and Clegg and Briblecombe [7] were all combined for the derivation of a self-consistent database of thermodynamic data of sulfuric acid. The work is being extended for application to hydrogen iodide thermodynamic data. The model is developed using the GAMS modeling framework. Analytical expressions have been calculated for all the partial derivatives, since GAMS cannot calculate derivatives. The regression program is developed in a way that it is open to additions of newer data to the database without the need for changing the main code. The development discussed above focuses on sulfuric acid data, but the equations and considerations for application to the hydrogen iodide data is analogous. Application of the described code for the development of a self consistent database of thermodynamic data of sulfuric acid and hydrogen iodide is currently being undertaken.

The method has been applied to aqueous solutions of sulfuric acid for which severe inconsistencies have been identified in the available thermodynamic data. The experimental data used for data reduction are given in Tables 3 and 4; a large composition and temperature range is covered, yet not up to the temperatures of the SI process. An example of the data inconsistency is shown in Figure 50, where vapor pressure data from different sources are plotted showing that there is a significant disagreement between the measured vapor pressures and the azeotropic point. In Figure 50 the reduced data (shown with lines) are displayed. The calculated values for the vapor pressure are in thermodynamic consistency with all other different types of data for the aqueous sulfuric acid solution (Table 3).

Table 3: Sources of experimental data

Temp Range (K)	Composition ($x_{H_2SO_4}$)	Species analyzed	Method	Reference
298.15	4.5 10^{-7}–0.139415	H_2SO_4-H_2O	$\Delta H_{mix}/RT$	[46]
298.15	5.6416 10^{-5}–0.0009	H_2SO_4-H_2O	$\Delta H_{mix}/RT$	[22]
298.15	0.02–0.9983	H_2O	$\Delta H_{mix}/RT$	[21]
303.15–598.15	0.005–0.8571	H_2SO_4	$\Delta H_{mix}/RT$	[31]
298.15	0.1013–0.9605	H_2SO_4-H_2O	Cp/R	[21]
253.15	0.3066–0.7517	H_2SO_4-H_2O	Cp/R	[21]
298.15	0.0009–0.01	H_2SO_4-H_2O	Cp/R	[23]
298.15	0.001–0.04	H_2SO_4-H_2O	Cp/R	[36]
283.15, 298.15, 313.15, 328.15	0.00186–0.0179	H_2SO_4-H_2O	Cp/R	[18]
293.15	0.0006–1 (100wt%)	H_2SO_4-H_2O	Cp/R	[21]
273.15–623.15	0–0.999	H_2SO_4-H_2O-SO_3	Vapor Pressure	[13]
273.15–673.15	0–0.999	H_2SO_4-H_2O-SO_3	Vapor Pressure	[10]
273.15–443.15	0–0.999	H_2SO_4-H_2O-SO_3	Vapor Pressure	[4]

Table 4: Summary of available experimental data

Property	Composition Range	Temperature Range(K)
$\Delta H_{dilution}/RT$	1.8 10^{-5}–9.15 10^{-4}	298.15
$\Delta H_{H_2O}/RT$	5.5 10^{-3}–0.9969	298.15
Cp/R	0.02–0.9983	182.15–315.15
$Cp_{H_2SO_4}/RT$	1.86 10^{-3}–0.25	181.74–328.15
P	0.02–1	273.15–793.15

More details and detailed illustrations of the thermodynamic data reduction framework developed to address the particular problems of the aqueous solutions of interest in the SI process can be found in a paper being prepared for publication.

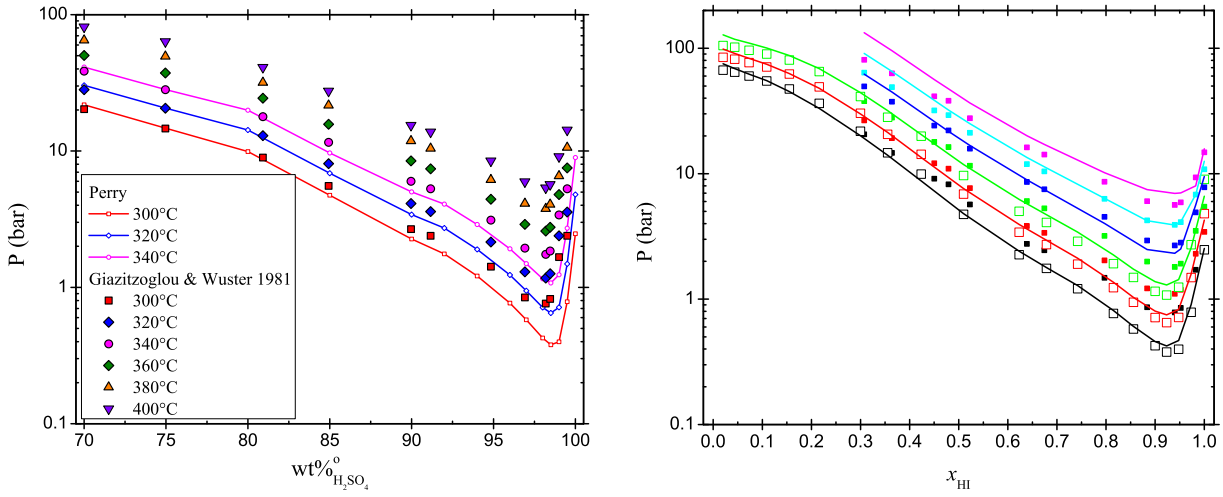

Figure 50: Thermodynamic data inconsistency and data reduction for the vapor pressure of the H_2SO_4-H_2O solution.

The binaries of HI and I_2 with water and the ternary of HI-H_2O-I_2 are even more challenging. Experimental data exist for the binary and ternary mixtures as shown in Table 5. The data reduction framework should be capable of handling liquid–liquid equilibrium as well as solid-liquid equilibrium, and this extension of the code is currently under development.

Table 5: Thermodynamic data for H_2O, HI and I_2

Solution studied	Measurement type	Reference
H_2O-HI	VLE	[47]
H_2O-HI	VLE	[39]
H_2O-HI	VLE	[9]
H_2O-HI	VLE	[17]
H_2O-HI	LLE	[33]
H_2O-HI	LLE	[14]
H_2O-HI	H^E	[44]
H_2O-I_2	LLE	[20]
H_2O-I_2	SLE	[20]
H_2O-I_2	SLE	[34]
H_2O-HI-I_2	VLE	[33]
H_2O-HI-I_2	VLE	[17]

The GAMS code, the experimental and reduced databases can be found online at

http://web.mit.edu/bollas/Public/ThermoData/. We plan on having all the results and original data accessible, so they can be updated with newer experimental results.

5 Publications from this NERI Project

1. G.M. Bollas, P.I. Barton and A. Mitsos. Bilevel Optimization Formulation for Parameter Estimation in Vapor-Liquid(-Liquid) Phase Equilibrium Problems. *Chemical Engineering Science*, 64(8), 1768–1783 2009.

2. G.M. Bollas, C.C. Chen, and P.I. Barton. Refined electrolyte-NRTL model: Inclusion of hydration for the detailed description of electrolyte solutions. Part I. Single electrolytes up to moderate concentrations, single salts up to the solubility limit. *Fluid Phase Equilibria*, in review, 2009.

3. A. Mitsos, G.M. Bollas, and P.I. Barton. Bilevel Optimization Formulation for Parameter Estimation in Liquid-Liquid Phase Equilibrium Problems. *Chemical Engineering Science*, 64(3), 548–559, 2009.

4. G.M. Bollas, C.C. Chen, and P.I. Barton. Refined Electrolyte-NRTL Model: Activity Coefficient Expressions for Application to Multi-Electrolyte Systems. *AIChE Journal*, 54(6), 1608–1624, 2008.

5. A. Mitsos and P.I. Barton. A Dual Extremum Principle in Thermodynamics. *AIChE Journal*, 53(8):2131–2147, 2007.

Conference Proceedings:

6. P.D. Ramirez-Munoz, M.S. Kazimi, P.I. Barton. Dynamic Simulation of Nuclear Hydrogen Production. *International Symposium on Process Systems Engineering, 16-20 Aug. 2009, Brazil.*

7. A. Mitsos, G.M. Bollas, P.I Barton. Parameter Estimation for Phase Equilibrium Models, *SIAM Computational Science and Engineering Conference, 2-6 Mar 2009, Miami, FL, USA.*

8. A. Mitsos, G.M. Bollas, P.I Barton. Model and Parameter Identification in Phase Equilibria, *ESCAPE 19, 14-19 June, Cracow, Poland.*

9. E. Choi, G.M. Bollas, P.I. Barton. Development of a self-consistent database of thermodynamic properties of sulfuric acid and hydrogen iodide in a wide range of composition, temperature and pressure, *AIChE Annual Meeting, 15-21 Nov. 2008, Philadelphia.*

10. G.M. Bollas, A. Mitsos, P.I. Barton. What Is the Number of Phases Predicted by Local Composition Models? Accurate Models Used In Inappropriate Ways. *AIChE Annual Meeting, 15-21 Nov. 2008, Philadelphia.*

11. G.M. Bollas, C.C Chen, P.I. Barton. Refined Electrolyte-NRTL Model: Inclusion of Hydration for the Detailed Description of Electrolyte Solutions, *AIChE Annual Meeting, 15-21 Nov. 2008, Philadelphia.*

12. G.M. Bollas, P. Smadbeck, P.I. Barton. Simulation of Flowsheet Options for the HI Concentration and Decomposition Section of the Sulfur-Iodine Thermochemical Cycle. *AIChE Annual Meeting, 15-21 Nov. 2008, Philadelphia.*

13. A. Mitsos, G.M. Bollas, P.I. Barton. Parameter Estimation for Phase Equilibrium Problems Via Bilevel Programs. *AIChE Annual Meeting, 15-21 Nov. 2008, Philadelphia.*

14. P.D. Ramirez-Munoz, M.S. Kazimi, and P.I. Barton. Simplification of the Inviscid Navier-Stokes Equations for Dynamic Simulation of Nonisothermal Gas Flow Networks. *AIChE Annual Meeting, 15-21 Nov. 2008, Philadelphia.*

15. P.D. Ramirez-Munoz, M.S. Kazimi, and P.I. Barton. Dynamic Simulation of a Coupled Heat Transfer Loop and a Nuclear Reactor In a Nuclear Hydrogen Plant. *AIChE Annual Meeting, 15-21 Nov. 2008, Philadelphia.*

16. P.I. Barton, G.M. Bollas, P. Ramirez-Munoz, M.S. Kazimi. Dynamic Simulation of Nuclear Hydrogen Production Processes, *2008 Indo-American Frontiers of Engineering Symposium, National Academy of Engineering of the National Academies, Irvine, CA, USA, 28 Feb - 1 Mar 2008.*

17. G.M. Bollas, C.C. Chen, and P.I. Barton. The Significance of Mixing Rules, Hydration and Complex Formation in the electrolyte NRTL Model. *AIChE Annual Meeting, 4-9 Nov. 2007, Salt Lake City.*

18. G.M. Bollas, M.S. Kazimi, and P.I. Barton. Detailed Modeling of the Thermodynamics of the Sulfur-Iodine Thermochemical Cycle. *AIChE Annual Meeting, 4-9 Nov. 2007, Salt Lake City.*

19. A. Mitsos and P.I. Barton. A Dual Stability Criterion in Phase Equilibria. *AIChE Annual Meeting, 4-9 Nov. 2007, Salt Lake City.*

20. P.D. Ramirez-Munoz, M.S. Kazimi, and P.I. Barton. Dynamic Simulation of the Heat Transfer Loop in a Nuclear Hydrogen Production Plant. *AIChE Annual Meeting, 4-9 Nov. 2007, Salt Lake City.*

Papers in preparation:

21. G.M. Bollas, C.C. Chen, and P.I. Barton. Refined electrolyte-NRTL model: Inclusion of hydration for the detailed description of electrolyte solutions. Part II. Detailed simulation of speciation and activities of aqueous solutions of acids and bases. *To be submitted to: Fluid Phase Equilibria*, 2009.

22. G.M. Bollas, E. Choi, and P.I. Barton. Reduced database and thermodynamic modeling of the Sulfur-Iodine thermochemical cycle: I. Development of self-consistent thermodynamic databases for aqueous sulfuric acid and hydrogen iodide. *To be submitted to: International Journal of Hydrogen Energy*, 2009.

23. G.M. Bollas and P.I. Barton. Reduced database and thermodynamic modeling of the Sulfur-Iodine thermochemical cycle: II. Detailed thermodynamic modeling of aqueous solutions of sulfuric acid and hydrogen iodide. *To be submitted to: International Journal of Hydrogen Energy*, 2009.

24. P.D. Ramirez-Munoz, M.S. Kazimi, and P.I. Barton. Dynamic Simulation of the Heat Transfer Loop in a Nuclear Hydrogen Production Plant. *To be submitted to: Nuclear Technology, 2009.*

5.1 Awards Received:

- Patricio Ramirez-Munoz won the Student Presentation Award from the Nuclear Engineering Division of *AIChE* at the *AIChE* 2008 Annual Meeting for his paper "Dynamic Simulation of a Coupled Heat Transfer Loop and a Nuclear Reactor In a Nuclear Hydrogen Plant"

- MSRP student Eugene Choi, who was working with Dr. George Bollas over summer 2008, received the first place award in the Fuels, Petrochemicals and Energy Section of the Undergraduate Student Poster Competition, at the *AIChE* 2008 National Student Conference for her paper entitled "Development of a Self-Consistent Database of Thermodynamic Properties of Sulfuric Acid and Hydrogen Iodide in a Wide Range of Composition, Temperature and Pressure."

References

[1] George M. Bollas, Paul I. Barton, and Alexander Mitsos. Bilevel optimization formulation for parameter estimation in vapor-liquid(-liquid) phase equilibrium problems. *Chemical Engineering Science*, 64(8):1768–1783, 2009.

[2] G.M. Bollas, C.C. Chen, and P.I. Barton. Refined electrolyte-NRTL model: Activity coefficient expressions for application to multi-electrolyte systems. *AIChE Journal*, 54(9):1608–1624, 2009.

[3] P. Bolsaitis and J. F. Elliott. Thermodynamic activities and equilibrium partial pressures for aqueous sulfuric acid solutions. *Journal of Chemical and Engineering Data*, 35(1):69–85, 1990.

[4] A. Bosen and H. Engels. Description of the phase equilibrium of sulfuric acid with the NRTL equation and a solvation model in a wide concentration and temperature range. *Fluid Phase Equilibria*, 43(2-3):213–220, 1988.

[5] L. C. Brown, R. D. Lentsch, G. E. Besenbruch, K. R. Schultz, and J. E. Funk. Alternative flowsheets for the sulfur-iodine thermochemical hydrogen cycle. Technical Report GAA24266, General Atomics, 2003.

[6] C.C. Chen and L.B. Evans. A Local Composition Model for the Excess Gibbs Energy of Aqueous Electrolyte Systems. *AIChE Journal*, 32(3):445, 1986.

[7] S. L. Clegg and P. Brimblecombe. Application of a Multicomponent Thermodynamic Model to Activities and Thermal Properties of 0-40 mol kg-1 Aqueous Sulfuric Acid from <200 to 328 K. *Journal of Chemical and Engineering Data*, 40(1):43–64, 1995.

[8] C.B. Davis, R. B. Barner, S. R. Sherman, and D. F. Wilson. Thermal-hydraulic analyses of heat transfer fluid requirements and characteristics for coupling a hydrogen product plant to a high-temperature nuclear reactor. Technical report, Idaho National Laboratory, 2005.

[9] H. Engels and K. F. Knoche. Vapor pressures of the system $HI/H_2O/I_2$ and H_2. *Int. J. Hydrogen Energy*, 11(11), 1986.

[10] Z. Giazitzouglou and G. Wüster. Das Binare System H_2SO_4; $P-V-T$ – Daten und Dampfdruckkurven in Weiten Konzentrationsbereichen bei erhohtem. *Druck. Ber. Bunsen-Ges. Phys. Chem.*, 85:127–132, 1981.

[11] J. Gmehling and U. Onken. *Vapor liquid equilibrium data collection/Pt. 1. Aqueous-organic systems*, volume 1, Part 1. DECHEMA, Deutsche Gesellschaft für Chemisches Apparatewesen, Chemische Technik und Biotechnologie eV, 1977.

[12] J. I. Gmitro and T. Vermeulen. Vapor-liquid equilibria for aqueous sulfuric acid. *AIChE Journal*, 10:740–746, 1964.

[13] D. W. Green and R. H. Perry. *Perry's Chemical Engineers' Handbook*. McGraw-Hill, New York, 2007.

[14] R. Haase, H. Naas, and H. Thumm. The thermodynamic behaviour of concentrated hydrohalic acids. *Z. Physik. Chem.*, 37:210–229, 1963.

[15] R. A. Heidemann and J. M. Mandhane. Some properties of the NRTL equation in correlating liquid-liquid equilibrium data. *Chemical Engineering Science*, 28(5):1213–1221, 1973.

[16] R.A. Heidemann and J.M. Mandhane. Some properties of the NRTL equation in correlating liquid–liquid equilibrium data. *Chemical Engineering Science*, 28:1213–1221, 1973.

[17] Masatoshi Hodotsuka, Xiaoyong Yang, Hiroyuki Okuda, and Kaoru Onuki. Vapor–Liquid Equilibria for the HI + H_2O System and the HI + H_2O + I_2 System. *Journal of Chemical & Engineering Data*, 53(8):1683–1687, 2008.

[18] J. K. Hovey and L. G. Hepler. Thermodynamics of sulphuric acid: apparent and partial molar heat capacities and volumes of aqueous H_2SO_4 from 10–55°C and calculation of the second dissociation constant to 350 C. *Journal of the Chemical Society, Faraday Transactions*, 86(16):2831–2839, 1990.

[19] E. Hückel. The theory of concentrated, aqueous solutions of strong electrolytes. *Physikalische Zeitschrift*, 26:93–147, 1925.

[20] F. C. Kracek. Solubilities in the System Water-Iodine to 200°C. *The Journal of Physical Chemistry*, 35(2):417–422, 1931.

[21] J. E. Kunzler and W. F. Giauque. Aqueous Sulfuric Acid. Heat Capacity. Partial Specific Heat Content of Water at 25 and-20. *J. Am. Chem. Soc*, 74(14):3472–3476, 1952.

[22] E. Lange, J. Monheim, and A. L. Robinson. The Heats of Dilution of Aqueous Solutions of Zinc, Cadmium and Copper Sulfates and Sulfuric Acid at 25°C. *Journal of the American Chemical Society*, 55(12):4733–4744, 1933.

[23] J. W. Larson, K.G. Zeeb, and L. G. Hepler. Heat capacities and volumes of dissociation of phosphoric acid (1st, 2nd, and 3rd), bicarbonate ion, and bisulfate ion in aqueous solution. *Canadian Journal of Chemistry*, 60(16):2141–2150, 1982.

[24] R. J. Leveque. *Finite Volume Methods for Hyperbolic Problems*. Cambridge University Press, Cambridge, UK, 2002.

[25] E. A. Macedo and P. Rasmussen. *Liquid-liquid equilibrium data collection*. DECHEMA, Deutsche Gesellschaft für Chemisches Apparatewesen, Chemische Technik und Biotechnologie e.V., 1987.

[26] J. N. Mandhane and R. A. Heidemann. Fitting activity-coefficients to vapor-liquid-equilibrium data. *Canadian Journal of Chemical Engineering*, 52(5):679–681, 1974.

[27] Y. Marcus and A. Rashin. A Simple Empirical Model Describing the Thermodynamics of Hydration of Ions of Widely Varying Charges, Sizes, and Shapes. *Biophysical chemistry*, 51(2-3):111–127, 1994.

[28] W.S. Martinson and P.I. Barton. Index and characteristic analysis of linear PDAE systems. *SIAM Journal on Scientific Computing*, 24:905, 2003.

[29] P. M. Mathias. Applied thermodynamics in chemical technology: current practice and future challenges. *Fluid Phase Equilibria*, 228:49–57, 2005.

[30] A.C. Mattelin and L.A.J. Verhoeye. The correlation of binary miscibility data by means of the N.R.T.L. equation. *Chemical Engineering Science*, 30(2):193–200, 1975.

[31] S. Milioto and J. M Simonson. 48^{th} Calorimeter Conference. *Durham NC*, 1993.

[32] Alexander Mitsos, George M. Bollas, and Paul I. Barton. Bilevel optimization formulation for parameter estimation in liquid-liquid phase equilibrium problems. *Chemical Engineering Science*, 64(3):548–559, 2009.

[33] G. Neumann. *$P-V-T$ und Dampfdruckmessungen zur Bestimmung thermodynamischer Eigenschaften starker Elektrolyte bei erhöhtem Druck*. PhD thesis, RWTH Aachen, 1987.

[34] D. R. O'Keefe and J. H. Norman. Vapor pressure, iodine solubility, and hydrogen solubility of hydrogen iodide-iodine solutions. *Journal of Chemical and Engineering Data*, 27(1):77–80, 1982.

[35] K. S. Pitzer. Electrolytes. From dilute solutions to fused salts. *Journal of the American Chemical Society*, 102(9):2902–2906, 1980.

[36] M. Randall and M. D. Taylor. Heat Capacity and Density of Aqueous Solutions of Potassium Iodate, Potassium Acid Sulfate, Iodic Acid, and Sulfuric Acid at 25°C. *The Journal of Physical Chemistry*, 45(6):959–967, 1941.

[37] H. Renon and J.M. Prausnitz. Local compositions in thermodynamic excess functions for liquid mixtures. *AIChE Journal*, 14(1):135–144, 1968.

[38] L. K. Rihko-Struckmann, J. A. Linnekoski, A. O. I. Krause, and O. S. Pavlov. Vapor-Liquid and Chemical Reaction Equilibria in the Synthesis of 2-Methoxy-2-methylbutane (TAME). *J. Chem. Eng. Data*, 45(6):1030–1035, 2000.

[39] T. Sako, T. Hakuta, and H. Yoshitome. *Kagaku Gijutsu Kenkyusho Hokoku*, 199:80–86, 1985.

[40] M. Shirvani and J.W.H. So. Solutions of Linear Differential Algebraic Equations. *SIAM Review*, 40:344, 1998.

[41] L.D. Simoni, Y. Lin, J.F. Brennecke, and M.A. Stadtherr. Reliable computation of binary parameters in activity coefficient models for liquid–liquid equilibrium. *Fluid Phase Equilibria*, 255(2):138–146, 2007.

[42] Sørensen, J.M. and Arlt, W. *Liquid-liquid Equilibrium Data Collection: Binary Systems*. DECHEMA, Deutsche Gesellschaft fur Chemisches Apparatewese, Chemische Technik und Biotechnologie eV, 1979.

[43] D. Tassios. The Number of Roots in the NRTL and LEMF Equations and the Effect on Their Performance. *Industrial & Engineering Chemistry Process Design and Development*, 18(1):182–186, 1979.

[44] C. Vanderzee and L. Gier. The enthalpy of solution of gaseous hydrogen iodide in water, and the relative apparent molar enthalpies of hydriodic acid. *J. Chem. Thermodyn*, 6:441, 1974.

[45] C. Wang. *Design, Analysis and Optimization of the Power Conversion System for the Modular Pebble Bed Reactor System*. PhD thesis, Massachusetts Institute of Technology, 2003.

[46] Y. C. Wu and T. F. Young. Enthalpies of dilution of aqueous electrolytes: sulfuric acid, hydrochloric acid, and lithium chloride. *J. Res. Natl. Bur. Stand.(US*, 85(1), 1980.

[47] G. Wüster. *$P - V - T$ und Dampfdruckmessungen zur Bestimmung thermodynamischer Eigenschaften starker Elektrolyte bei erhöhtem Druck*. PhD thesis, Rheinisch-Westfälische Technische Hochschule Aachen, 1979.

[48] F. J. Zeleznik. Thermodynamic Properties of the Aqueous Sulfuric Acid System to 350 K. *Journal of Physical and Chemical Reference Data*, 20:1157, 1991.